ARTICLE

Origin of Palaeoproterozoic, sub-seafloor Zn-Pb-Ag skarn deposits, Sala area, Bergslagen, Sweden

Nils F. Jansson[1] · Rodney L. Allen[2] · Göran Skogsmo[3] · Thomas Turner[1]

Abstract

Unravelling the genesis of metamorphosed mineral deposits can be complicated due to difficulties in separating between primary features and features that formed during the metamorphic overprint. Such uncertainty exists for stratabound and dolomite- and skarn-hosted Zn-Pb-Ag sulfide deposits in 1.89 Ga rocks in the Bergslagen lithotectonic unit (BLU) of Sweden, where a metasomatic vs. regional metamorphic origin for skarns has long been discussed. By integrating geological mapping with new lithogeochemical, mineralogical, and stable isotope data (C, O, S), we show that complexly zoned garnet and clinopyroxene skarns in the Sala area of the central BLU predate mineralization. Sphalerite-galena mineralization formed after the deposition of a younger, more Mn-rich ferroan diopside and andradite-grossular garnet, and is associated with phlogopite, tremolite-actinolite, chlorite, serpentine, and calcite. Mineralization in conjunction with a transition from high-T metasomatism to hydrolytic alteration is inferred. An average $\delta^{34}S_{V\text{-}CDT}$ of $1.6 \pm 1.9\text{‰}$ in sulfides is consistent with a primordial sulfur source. Trends defined by negative shifts in $\delta^{18}O_{V\text{-}SMOW}$ and $\delta^{13}C_{V\text{-}PDB}$ in dolomite and calcite are consistent with fluid infiltration at 300–500 °C. The alteration system is sharply truncated by unaltered, c. 1.89 Ga calc-alkaline granite and porphyritic intrusions, which along with F_1 folding of the alteration zones and mineralization suggest that mineralization predate regional metamorphism. The Sala deposits are interpreted as Zn skarn deposits formed in conjunction with the emplacement of intrusions into penecontemporaneous marine volcanic and dolomitized limestone strata. The unusually Mg-rich mineralogy in relation to Zn skarns worldwide most likely reflects the dolomitic precursor.

Introduction

The systematic study of skarns minerals, their fluid inclusions, and their spatial and temporal zonation patterns can be used to model the physiochemical characteristics of skarn-forming hydrothermal systems (Harris and Einaudi 1982; Newberry et al. 1991), vector in on skarn deposits (Meinert 1987; Meinert et al. 2005), and locally date them (Burisch et al. 2019). This hinges on fundamental temporal

and spatial relationships between ore and skarn minerals, allowing inferences on ore-forming processes to be drawn from non-ore minerals such as garnet, clinopyroxene, and amphibole. This approach is more complicated to apply to mineral deposits that have been modified by ductile deformation and regional metamorphism, where it can be difficult to separate primary features from secondary modifications. Minerals like garnet, clinopyroxene, and amphibole can for example form by metamorphic reactions between silicates, iron oxides, and carbonates in banded iron formations (e.g. Klein 1973), presenting an obvious scenario where current mineralogy carry little if any direct information on original ore-forming processes. In more extreme cases, garnet- and pyroxene-bearing deposits in amphibole to granulite facies metamorphic belts can stimulate decades of ore genetic controversies, such as the long-lived discussions on the syngenetic vs. epigenetic models for Broken Hill and similar deposits (see Spry and Teale (2021) for a recent review). Besides affecting our understanding of the secular distribution of specific deposit types, such uncertainties impact on how and where we explore for Zn deposits, a non-trivial

✉ Nils F. Jansson
niljan@ltu.se

1 Division of Geosciences and Environmental Engineering, Department of Civil, Environmental and Natural Resources Engineering, Luleå University of Technology, 97187 Luleå, Sweden

2 Volcanic Resources AB, Timotejvägen 18, 74948 Enköping, Sweden

3 Björka Mineral AB, 705 97 Glanshammar, Sweden

matter given that some of the world's largest Zn deposits are complex, exotic deposits in ancient orogens (Sangster 2020). In-depth studies are commonly needed to unravel fundamental ore genetic controls for these deposits, and to better tailor exploration models towards new discoveries in complex terrains.

Stratabound Zn-Pb-Ag sulfide deposits in dolomite, skarn, and hydrothermally altered and metamorphosed volcanic rocks occur in the Bergslagen lithotectonic unit (BLU), one of the major building blocks of the 2.0–1.8 Ga Svecokarelian orogen in the Fennoscandian shield (Fig. 1). Notable deposits include the 28.1 Mt Falun deposit, the 6.7 Mt Stollberg ore field, and the currently mined > 144 Mt Garpenberg deposit (Stephens and Jansson 2020), one of the largest zinc mines in the world. A long history of polyphase ductile deformation and medium-grade regional metamorphism complicate ore genetic studies and classification. Geochronologic and stratigraphic evidence have shown that these deposits formed synvolcanically at c. 1.89 Ga, when hydrothermal fluids replaced limestone interbeds in a marine volcanic succession of mainly felsic composition (Allen et al. 1996; Jansson et al. 2013; Kampmann et al. 2017). Broadly syngenetic timing, submarine volcanic setting, and the style and composition of associated alteration zones in felsic volcanic rocks comprise similarities to metamorphosed, subseafloor replacement volcanogenic massive sulfide (VMS) deposits (Doyle and Allen 2003; Franklin et al. 2005; Tornos et al. 2015). On the contrary, the deposits are commonly marble-hosted, and accompanied by skarns rich in clinopyroxene, amphibole, garnet, and olivine. A key question for research is whether the deposits should be regarded as an atypical form of skarn deposit formed in ancient marine volcanic systems (Jansson and Allen 2015), or whether the skarn minerals are merely a metamorphic overprint.

Recent detailed studies at Falun (Kampmann et al. 2017) and Garpenberg (Jansson and Allen 2013, 2015) indicate that skarns in these deposits may have begun forming already in conjunction with ore formation at c. 1.89 Ga, prior to subsequent regional metamorphism. However, a limitation of these studies is that they were conducted in parts of the BLU where regional metamorphism attained amphibole facies, complicating detailed interpretation.

In contrast, marble- and skarn-hosted Zn-Pb-Ag deposits in the Sala area occur in a part of the BLU where regional metamorphism only attained upper greenschist facies, and where the degree of ductile deformation is lower (Ripa et al. 2002; Allen et al. 2003). Despite potentially holding keys to better understanding the genesis of skarns in Bergslagen, the Sala deposits have been the subject of few modern studies. The most comprehensive descriptions were published a century ago by Sjögren (1910) and Tegengren (1924). Modern work is restricted to a study of Ag, Hg, and Sb minerals in ore by Kieft et al. (1987), a 1:50,000 bedrock map by Ripa

et al. (2002), and a sedimentary facies analysis of the marble host by Allen et al. (2003). These previous studies present only fragmentary information on the style and setting of the deposits and their associated alteration. In particular, there is shortage of data on the skarn minerals.

A structural geological study by Jansson (2017) interpreted the sulfide lenses at Sala mine to have formed by a combination of cross-stratal fluid flow in discordant breccia zones, and from lateral fluid flow along the contacts between the carbonate rock and volcanic interbeds in the succession, prior to ductile deformation and regional metamorphism. However, due to little published information on the relationship between ore and gangue silicates and the distribution, mineralogy, and geochemistry of altered rocks at Sala, the question regarding skarn genesis was left unresolved.

Against this background, a geological mapping and sampling campaign was conducted in 2017–2020, focused on documenting the main structural, stratigraphic, and alteration features of the Zn-Pb-Ag deposits. In this contribution, we combine these new geological mapping results with sampling of the Zn-Pb-Ag deposits and their host rock for whole-rock lithogeochemistry, mineral chemistry, and stable isotope (C, O, and S) geochemistry. We illustrate that the deposits and their associated skarns are best reconciled with infiltration metasomatism of high-temperature fluids already at the synvolcanic stage. This in turn impacts exploration strategies for similar deposits in the BLU, and for the exploration potential for Zn skarn deposits in the ancient carbonate-bearing successions globally.

Geological background

The Bergslagen lithotectonic unit

The BLU is one of the major building blocks of the Svecokarelian orogen in the Fennoscandian shield. It is separated from other lithotectonic units in the Svecokarelian orogen to the north and south by NW-trending ductile shear zones (Fig. 1; Stephens and Bergman 2020). The eastern extent is obscured by the Baltic sea and Phanerozoic cover rocks, whereas the western contact is marked by the front of the c. 0.95 Ga Sveconorwegian (Grenvillian) orogen. In the northwest, the BLU is intruded by younger igneous rocks and unconformably overlain by c. 1.7 Ga sedimentary rocks. The BLU is dominated by felsic plutonic rocks that formed between 1.9 and 1.75 Ga, during and after the Svecokarelian orogeny (Stephens et al. 2009; Stephens and Jansson 2020 and references therein). The earliest plutonic rocks consist of a suite of granite, granodiorite, diorite, and gabbro (GDG) emplaced at c. 1.91–1.87 Ga. The GDG suite intruded into a several kilometer-thick package of > 1.91–1.89 Ga mainly felsic volcanic rocks that is underlain and overlain by
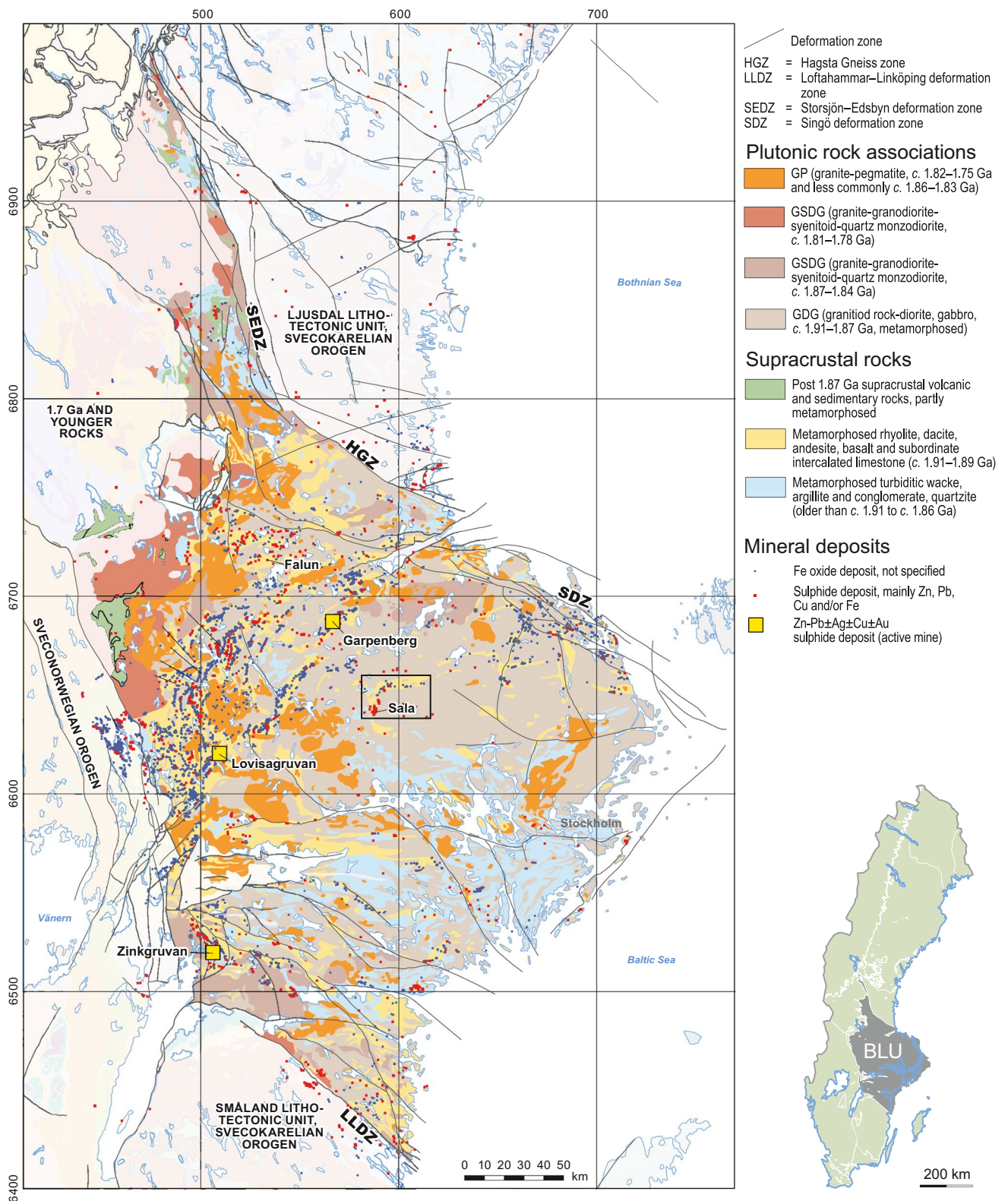
Fig. 1 Bedrock geological map of the Bergslagen lithotectonic unit (BLU), showing the distribution of polymetallic sulfide and iron oxide deposits. The dolomite marble host to the Sala Zn-Pb-Ag deposit is included in the map unit here termed 'metamorphosed rhyolite, dacite, andesite, basalt and subordinate interacalated limestone (c. 1.91 Ga-1.89 Ga)'. Inset shows the location of the BLU in Sweden. The Sala inlier as shown in Fig. ESM1 is outlined. Modified after Stephens and Jansson (2020)
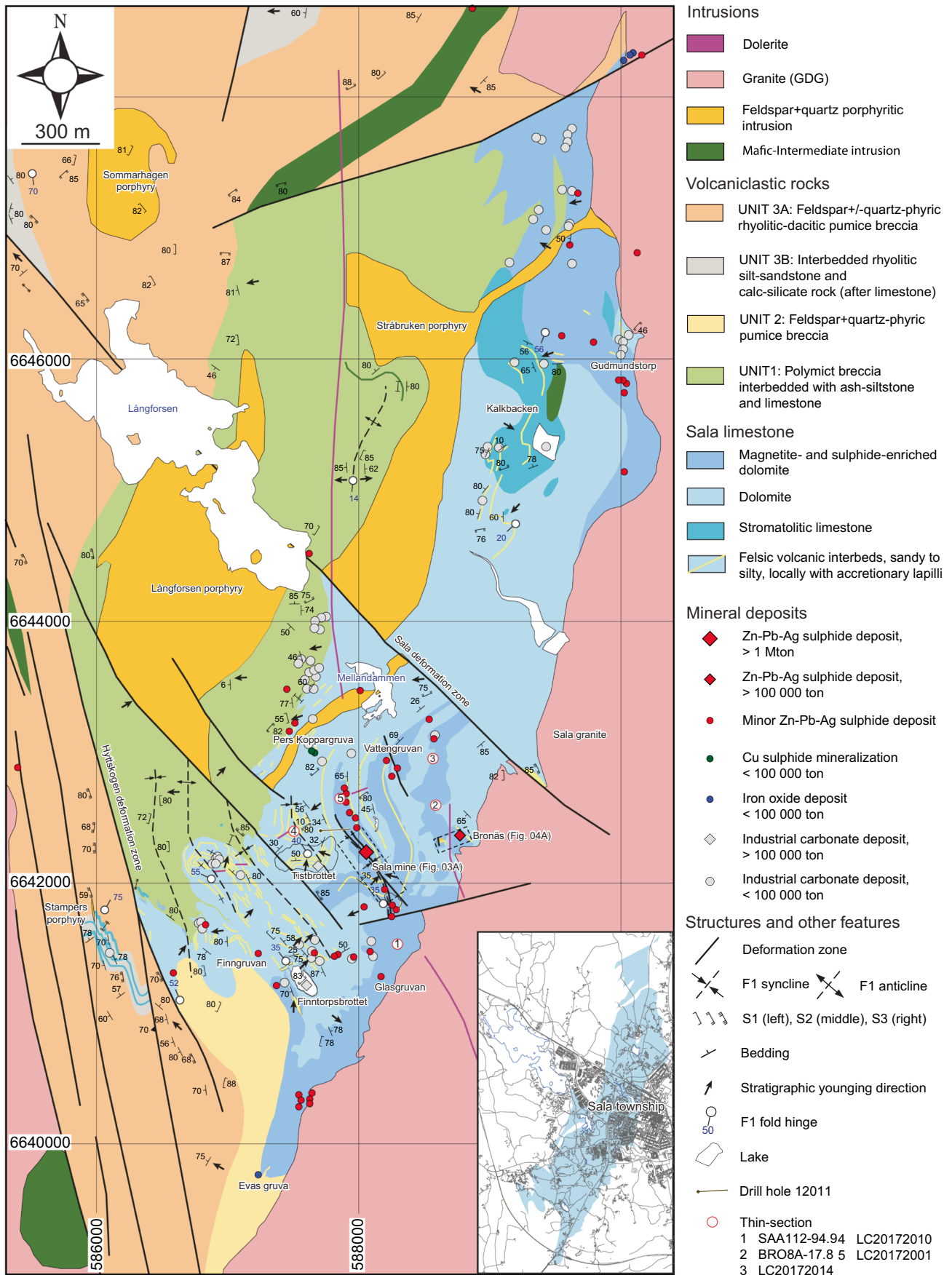
Intrusions

- Dolerite
- Granite (GDG)
- Feldspar+quartz porphyritic intrusion
- Mafic-Intermediate intrusion

Volcaniclastic rocks

- UNIT 3A: Feldspar+/-quartz-phyric rhyolitic-dacitic pumice breccia
- UNIT 3B: Interbedded rhyolitic silt-sandstone and calc-silicate rock (after limestone)
- UNIT 2: Feldspar+quartz-phyric pumice breccia
- UNIT1: Polymict breccia interbedded with ash-siltstone and limestone

Sala limestone

- Magnetite- and sulphide-enriched dolomite
- Dolomite
- Stromatolitic limestone
- Felsic volcanic interbeds, sandy to silty, locally with accretionary lapilli

Mineral deposits

- Zn-Pb-Ag sulphide deposit, > 1 Mton
- Zn-Pb-Ag sulphide deposit, > 100 000 ton
- Minor Zn-Pb-Ag sulphide deposit
- Cu sulphide mineralization < 100 000 ton
- Iron oxide deposit < 100 000 ton
- Industrial carbonate deposit, > 100 000 ton
- Industrial carbonate deposit, < 100 000 ton

Structures and other features

- Deformation zone
- F1 syncline   F1 anticline
- S1 (left), S2 (middle), S3 (right)
- Bedding
- Stratigraphic younging direction
- F1 fold hinge
- Lake
- Drill hole 12011
- Thin-section
  1 SAA112-94.94 LC20172010
  2 BRO8A-17.8 5 LC20172001
  3 LC20172014

◀**Fig. 2** New bedrock geological map of the Sala area based on outcrop mapping, drill core logging, and re-interpretation of older maps (Tegengren 1924; Ripa et al. 2002; Allen et al. 2003; Jansson 2007). The metavolcanic rocks and marble are here named according to the interpreted pre-metamorphic facies as determined from textural evidence. Grid is Swedish national grid SWEREF99TM. Infrastructure (roads, houses, railroad) related to Sala township is shown on top of the Sala limestone in the lower right inset. Particularly in the most densely populated area, outcrop exposure is close to zero, hence the low degree of detail in this part of the geological map. Drill hole 12,011 is collared 38 m below sea level (126 m below surface) with a plunge of 44° towards the east

siliciclastic sedimentary rocks (turbiditic wacke, argillite, conglomerate, and quartzite). Some of the GDG felsic plutons are interpreted to have been coeval and co-magmatic with the volcanic succession they intrude into, i.e. to be subvolcanic (Allen et al. 1996; Jansson and Allen 2011; Stephens and Jansson 2020).

Facies associations in the 1.91–1.89 Ga volcanic succession are indicative of a predominantly shallow marine depositional environment, and during pauses in volcanism, stromatolitic limestone interbeds formed (Allen et al. 1996). The tectonic environment at 1.91–1.87 has been interpreted as a marine back-arc or intra-arc basin on extended c. 2.1 Ga continental crust (Allen et al. 1996; Stephens et al. 2009; Stephens and Jansson 2020).

At c. 1.87–1.86 Ga, the rocks were subjected to ductile deformation (D_1), medium-grade regional metamorphism (M_1) including local migmatization, and the onset of emplacement of a younger plutonic suite consisting of granite, granodiorite, syenitoid, and quartz monzodiorite (GSDG, Fig. 1; Stephens and Jansson 2020). The driving agent for this tectonic cycle has been interpreted as migratory tectonic switching from extension to compression within an accretionary orogeny, inboard of an active continental margin (Hermansson et al. 2008; Stephens et al. 2009). At least two additional tectonic cycles from extension to compression have been inferred in the time range 1.86–1.75 Ga, associated with continued emplacement of GSDG plutonic rocks, local emplacement of post-1.87 Ga supracrustal rocks, a prominent phase of regional D_2 deformation and M_2 metamorphism at c. 1.84–1.80 Ga, and emplacement of anatectic granite-pegmatite (GP) at 1.85–1.83 Ga and 1.82–1.75 Ga. As a consequence of these events, supracrustal rocks belonging to the 1.91–1.89 Ga succession now occur as folded inliers enclosed by plutonic rocks (Fig. 1).

The numerous iron oxide and Zn-Pb-Ag sulfide deposits in the BLU show a clear spatial affinity to the 1.91–1.89 Ga metavolcanic rocks (Fig. 1), and in detail especially to the marble interbeds. This reflects the role of metamorphosed limestone interbeds in the volcanic succession as hosts for the principal types of iron oxide and sulfide deposits in the BLU, which are calcic and magnesian iron skarn deposits and SVALS-type deposits, respectively (Stephens and

Jansson 2020). It also reflects the presence of stratiform, syngenetic deposits, including banded iron formations and stratiform Zn-Pb-Ag sulfide deposits, which occur in stratigraphic intervals dominated by metamorphosed volcaniclastic siltstone and limestone (Allen et al. 1996). The latter type include the currently mined Zinkgruvan and Lovisa deposits, which were collectively referred to as 'stratiform ash-siltstone hosted Zn-Pb-Ag sulfide deposits' (SAS-type) by Allen et al. (1996). The SAS-type deposits have been interpreted as syngenetic-exhalative Zn-Pb-Ag deposits.

The Sala inlier

In the Sala area, rhyolitic-dacitic and subordinate basaltic metavolcanic rocks belonging to the 1.91–1.89 Ga supracrustal unit define a crescent-shaped inlier, bound on all sides by GDG plutonic rocks or deformation zones (Figs. 1, ESM1). A synthesis of structural stratigraphic relationships at inlier scale will be presented in a separation contribution (Jansson et al. in prep.). This section presents a summary of key relationships based on previous work, with focus on the study area (Fig. 2).

The oldest known metavolcanic rocks, including a felsic unit dated at 1906 ± 3 Ma, occur interbedded with quartzite and meta-arkose in the Broddbo area in the northwestern corner of the inlier (Fig. ESM1). Marble interbeds are abundant in the metavolcanic rocks along the inner edge of the inlier, including a thick, predominantly dolomitic marble unit at Sala, for which an origin as dolomitized stromatolitic limestone has been established (Fig. ESM1) (Collini 1965; Ripa et al. 2002; Allen et al. 2003; Jansson 2017). The majority of polymetallic sulfide deposits in the Sala inlier are hosted by the Sala marble, including the dolomite- and skarn-hosted, stratabound Zn-Pb-Ag sulfide deposits, which are the focus of this contribution. Volcaniclastic interbeds, ranging from a centimeter to a few meters thick, and ranging from laminated rhyolitic ash-siltstone to crystal-rich sandstone, are frequent in the limestone and commonly drape stromatolitic microtopography (Allen et al. 2003; Jansson 2007, 2017). A metavolcanic interbed with relict accretionary lapilli within the Sala marble unit yielded a U–Pb zircon age of 1894 ± 2 Ma (Stephens et al. 2009).

The supracrustal rocks are intruded by feldspar + quartz-porphyritic intrusions, interpreted by Ripa et al. (2002) as subvolcanic intrusions. A U–Pb zircon age of $1892 + 5/ - 4$ Ma was presented by Stephens et al. (2009) for one such unit in the northern part of the Sala marble (Fig. ESM1). Calc-alkaline granite of the GDG suite, directly east of the Sala inlier ('Sala granite'), is in contact with the dolomitic marble unit at Sala and has returned a U–Pb zircon age of 1891 ± 6 Ma (Ripa et al. (2002).

Ripa et al. (2002) showed that the Sala mine area is deformed by NNE-SSW to NW–SE trending F_1 folds,

whose axial surfaces are curved due to open S-symmetric F_2 folding around NE-SW to E-W trending axial surfaces. Interference of the relatively open F_1 and F_2 folds in the area has commonly resulted in non-cylindrical fold geometries with curved hinges (Jansson 2007, 2017). Absolute age constraints on F_1 and F_2 in the Sala area are lacking, but correlation with regional structures tentatively suggests a c. 1.87–1.86 Ga and a 1.84–1.81 Ga timing, respectively (Stephens and Jansson 2020). A WSW-dipping shear zone (the Hyttskogen deformation zone), with an inferred dextral and reverse sense of shear, forms the western boundary of the inlier (Fig. ESM1), and was interpreted as a D_3 structure by Ripa et al. (2002). Several steeply SW-dipping deformation zones occur also in the Sala area, e.g. the Sala deformation zone (Fig. ESM1). Jansson (2017) described dextral strike-slip faults of similar orientation in the Sala mine, where they offset WSW-ENE trending dolerite dykes belonging to a 1.6–1.56 Ga age suite, hence indicating that the faults were active long after the Svecokarelian orogeny. The youngest rocks are N-S trending dolerite dykes emplaced at 0.98–0.95 Ga (Söderlund et al. 2005), and which are not known to be affected by deformation in the Sala area.

Mineral deposits

Historic mining in the Sala area targeted high-grade massive to semi-massive sulfide bodies dominated by sphalerite and galena. The deposits comprised replacements and breccia infill within dolomite and skarn, commonly close to deformation zones or contacts between dolomite marble and felsic metavolcanic rock (Fig. 2). The majority of the mines were small ($< < 0.1$ Mt), with limited in situ material left for modern studies. This study will focus on the two largest deposits, Sala mine and Bronäs (Fig. 2). Complementary data have been collected at the small Glasgruvan Zn-Pb-Ag mine further south (Fig. 2). Sphalerite and galena were the main ore minerals at these deposits.

Jansson (2017) found that the Sala mine targeted a series of elongate, planar sulfide lenses which extend for ca. 1 km along NNW-SSE trend, and plunge approximately 35° towards NNW (Fig. 2, Fig. 3A). The mined sulfide lenses occurred in the hinge zone of the F_1 syncline and show parallel plunges with the syncline hinge plunging 35° towards the NNW (Fig. 3B). The plunge of mineralization is locally reversed by subordinate F_2 fold hinges in the mine (Fig. 3A). The hinge zone of the F_1 syncline is cross-cut by the Storgruveskölen shear zone (SSZ), a NNW-trending shear zone with strike parallel to the axial surface of the syncline (Jansson 2017). The SSZ commonly bordered massive sulfide mineralization and is rich in talc, chlorite, serpentine, and calcite. Although the mineralization as a whole is discordant to bedding (Fig. 2),

individual ore bodies are commonly parallel to altered volcanic interbeds that are cut by the SSZ (Fig. 3A).

The Bronäs deposit occurs closer to the Sala granite (Fig. 2). Re-logging of old drill cores and analysis of old mine maps (Heuberg, 1952) by Turner (2020) showed that mineralization occurred as several sub-parallel, discontinuous bodies, dipping 65–70° towards SSW (Fig. 4A-B). Similar to the situation at the Sala mine, stratabound mineralization is preferably developed in a part of the Sala limestone containing abundant felsic volcanic interbeds, and trends sub-parallel to these (Fig. 4B).

Kieft et al. (1987) described a plethora of minor to accessory minerals carrying Ag, Sb, and Hg in Zn-Pb-Ag mineralization from the Sala area. Silver was found to be mainly hosted by silver amalgam, sulphosalts, antimonides, and as the native metal, commonly as inclusions in sphalerite and galena. Detailed grade and tonnage data are not available due to insufficient historic production records and lack of formal resource estimates. Grip (1983) estimated that 5 Mt of ore and waste were mined at Sala mine, from which Tegengren (1924) reported average grades of 12% Zn, 2% Pb, 150–200 ppm Ag for sphalerite-dominated ore bodies. Mining at Bronäs during 1951–1962 produced 0.17 Mt of ore grading 4.2% Pb, 2.0% Zn, and 350 g/t Ag (Grip 1983).

Methods

Field mapping and drill core logging

To better understand the geological framework of the marble-hosted Zn-Pb-Ag deposits, the Sala area was re-mapped in detail with emphasis on structure, stratigraphy, and alteration (the resulting map is presented in Fig. 2). The area is characterized by a relatively low topographic relief and a Quaternary cover of till, glaciofluvial deposits, and clay. Boreal forest vegetation alternate with agricultural lands, and a considerable part of the study area is covered by urban infrastructure of the Sala township. Hence, outcrop exposure is subordinate in most areas, and bedrock composition generally cannot be deduced from the glacially transported overburden. However, glacial erosion means that the degree of weathering and oxidation is low, and mineralogically fresh samples could easily be obtained from outcrops.

Mapping was complemented by geological logging of ca. 2500 m of drill core in 19 exploration drill holes. Legacy data from earlier mapping, surveying, and sampling campaigns by the Geological Survey of Sweden (Ripa et al. 2002), Björka Mineral, Boliden Mineral, plus underground mapping in Sala mine by Jansson (2007) during creation of Fig. 2.
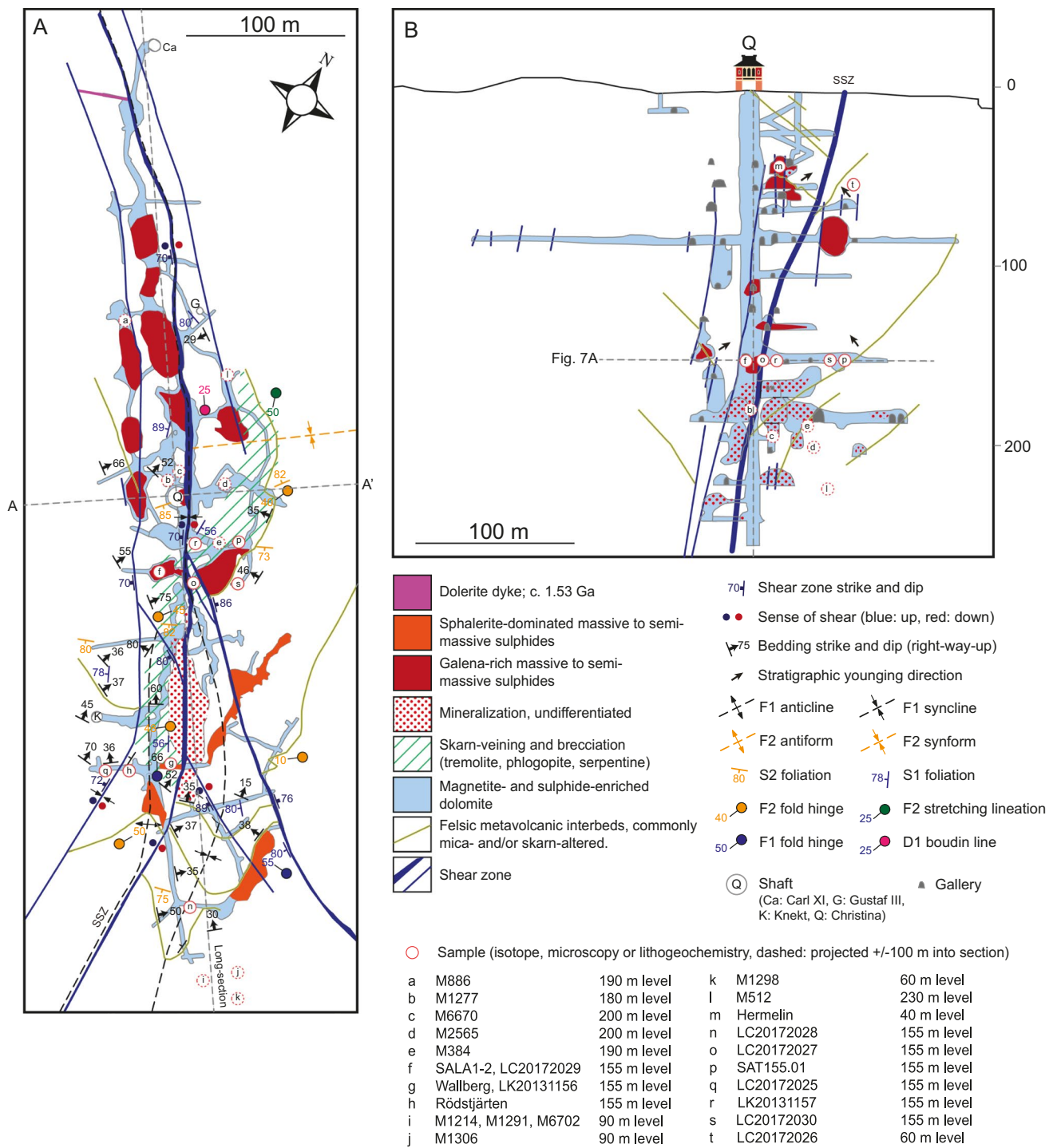
Fig. 3 (**A**) Geological map of the 155 m level in the Sala mine, based in underground mapping presented in Jansson (2017). (**B**) Geological cross-section (viewed NW) along the line A–A′. Mine outline and mineralization is based on Sjögren (1910). Dashed samples have been projected horizontally and vertically from adjacent sections. The area with undifferentiated mineralization is a collapsed sixteenth century part of the mine, for which no detailed information about the ore exists

Analytical methods

During mapping and logging, samples were collected for whole-rock lithogeochemistry ($N = 207$), polished thin sections ($N = 109$), carbon and oxygen isotopes ($N = 144$), and sulfur isotope analysis ($N = 27$). The description below is a short summary, whereas detailed descriptions of the analytical methods and quality assurance and quality
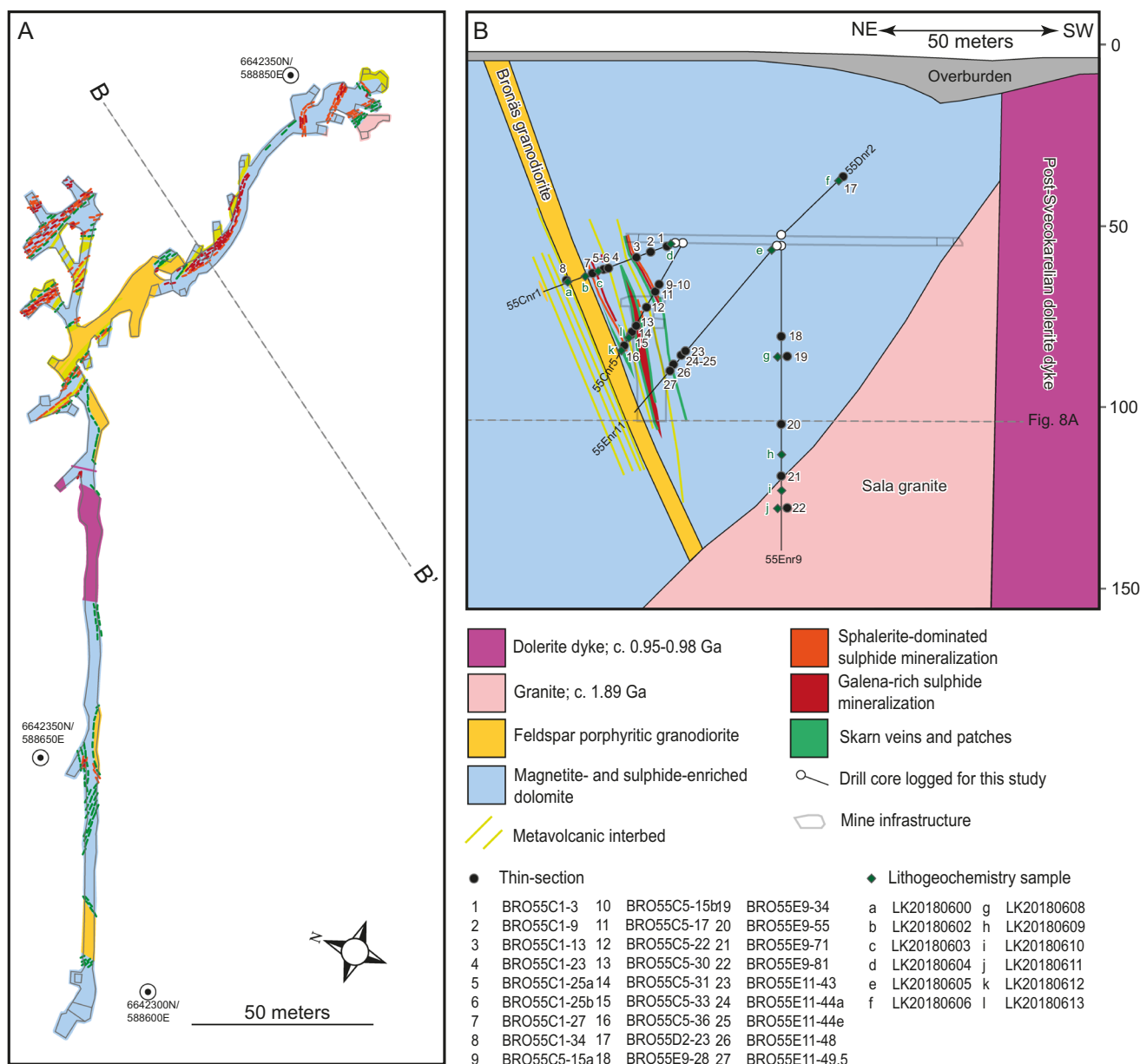
Fig. 4 A Geological map of the 105 m level in the Bronäs mine, digitized and re-interpreted after Heuberg (1952). (**B**) Geological cross-section viewed SW of the Bronäs deposit, based on maps in Heuberg (1952) and re-logging of indicated drill cores by Turner (2020). According to Grip (1983), Bronäs produced 171,000 tons of ore grading 4.2% Pb, 2.0% Zn, and 350 g/t Ag during the years 1951–1962

control (QA/QC) procedures are provided in the electronic supplementary materials (ESM2-3).

Whole-rock lithogeochemical analysis of samples of marble and metamorphosed intrusions was conducted at ACME Laboratories using inductively coupled plasma-emission spectroscopy (ICP-ES) and ICP-mass spectrometry (ICP-MS) following lithium metaborate fusion and nitric acid digestion. Total sulfur and carbon were determined by the Leco method. Ferrous iron was determined at ALS Vancouver using $K_2Cr_2O_7$ titration following H_2SO_4-HF digestion. All lithogeochemical data are compiled in ESM2 and ESM3.

The mineral chemistry of carbonates, silicates, magnetite, and sphalerite was determined in polished thin sections, using a Jeol JXA-8530F HyperProbe at Uppsala University (Sweden) and a Jeol JXA-8230 Electron Probe Microanalyzer at AGH University of Science and Technology (Kraków, Poland). All mineral chemical data and details of the analytical conditions are provided in ESM4.

Stable isotope analyses (C, O, and S) were conducted on 75–212 micron powdered carbonate, sulfides, and barite at the Institute of Applied Geosciences of Karlsruhe Institute of Technology (KIT), Germany. For C and O analyses in carbonates, samples were dissolved in phosphoric acid and passed through online carbonate preparation system (GasBenchII) linked to a delta advantage mass spectrometer (Thermo-Finnigan). Results are reported in the notation [‰] relative to the Vienna Pee Dee Belemnite (VPDB; $\delta^{13}C$) and Standard Marine Oceanic Water (VSMOW; $\delta^{18}O$) (see ESM5 for analytical data). Sulfur isotope samples were combusted at 1030 °C and resulting gases were separated using a GC column, prior to analysis using an Isoprime Isotope Ratio Mass Spectrometer (GV Instruments). Results are given in the notation [‰] relative to the Vienna Canyon Diablo Troilite (V-CDT) standard. All stable isotope data are compiled in ESM5.

Results

Structure and stratigraphy

Relict stromatolitic textures in many places testify to an origin by biogenic growth by cyanobacteria in a shallow marine environment (Fig. ESM6A). The volcaniclastic interbeds that drape the stromatolites function as excellent bedding markers, aiding determination of stratigraphic younging, and allowing the complex fold patterns on Fig. 2 to be mapped out. The results confirm that the area is characterized by gently plunging F_1 synclines and anticlines, with axial surfaces varying in strike from NW–SE to NNE-SSW (Fig. 2, see ESM7 for a cross-section). In plain view, F_1 folds near Sala mine are generally open and plunge gently towards N-NW, whereas to the north near Kalkbacken, F_1 folds display S-symmetries and have sub-horizontal or gently S-SE plunging fold hinges (Fig. 2). Observed outcrop scale structures associated with an E-W to SW-NE trending S_2 foliation are consistent with earlier inferences of F_2 folding as a cause of the non-cylindrical F_1 fold hinges and the curvature of F_1 axial surfaces.

The Hyttskogen deformation zone has deflected and transposed earlier structures into steeper orientations (e.g. measured F_1 fold hinges in Fig. 2). Dextral strike-slip offset is indicated for the Sala deformation zone, whereas west-side up displacement is suggested for the Hyttskogen deformation zone based on S-C, C'-S fabrics and offset lithological contacts. Foliations associated with these zones are termed S_3 on Fig. 2.

Deformation and metamorphism have commonly degraded primary rock textures. Using the facies analysis criteria of Allen et al. (1996), we constrained the pre-metamorphic protoliths. This is the basis for the unit division on Fig. 2, where metavolcanic and metasedimentary rocks are divided and named using descriptive, pre-metamorphic rock names that emphasize primary depositional facies. In light of evidence for a secondary origin for dolomite as presented in Ripa et al. (2002), the marble unit will be referred to as the Sala limestone in a lithostratigraphic context. The subdivisions into different marble varieties as depicted on Fig. 2 will be described in the sections on alteration.

Structural thickening due to the F_1-F_2 fold interference is likely the reason for the great surface extent of the Sala limestone. Structural complexity and the cutting character of the Sala granite (see below) makes determination of the original stratigraphic thickness of the Sala limestone difficult; however, it is estimated to be at least several hundred meters thick based on the map pattern on Fig. 2.

Stratigraphic younging indicators including normal grading, erosional contacts, cross-stratification, and stromatolite microtopography suggest the Sala limestone is stratigraphically overlain by, and appears to laterally interfinger with, a succession of rhyolitic volcanic breccia-conglomerate and rhyolitic silt-sandstone in the NW (UNIT 1 on Figs. 2 and ESM7). The breccia-conglomerate beds commonly contain clasts of both limestone and felsic volcanic rock and show basal contacts that are erosional into the substrate. The lithic fragments are generally blocky, subangular, and matrix-supported (Fig. ESM6B). The limestone fragments are variably replaced by calc-silicates, and commonly weathered out in outcrop. Calc-silicates commonly give a green tint to the breccia-conglomerate matrix, and calc-silicate bands locally accentuate sedimentary bedding in the rhyolitic silt-sandstone facies (Fig. ESM6C).

In the southwest part of the study area, the Sala limestone borders an approximately 300-m-thick unit of feldspar + quartz-phyric rhyolitic pumice breccia (UNIT 2, Fig. 2), which differs from UNIT 1 in absence of limestone fragments. Relict pumice clasts are locally up to 10 cm in size and carry a similar feldspar and quartz phenocryst population as the matrix (Fig. ESM6D). The contact with the Sala limestone is not exposed in outcrop or intersected by drilling, and consequently the nature of this contact could not be determined. However, it is inferred that the unit similarly to UNIT 1 overlies the Sala limestone based on younging directions (Fig. 2) and geochemical similarities to UNIT 1 (Jansson et al. in prep).

The units described above are stratigraphically overlain by a unit of rhyolitic-dacitic pumice breccia (UNIT 3A) with subordinate intervals of rhyolitic silt-sandstone and tremolite-clinozoisite-rich calc-silicate rock (UNIT 3B). Relict pumice clasts are common (Fig. ESM6E). The silt-sandstone beds locally show normal grading and cross-stratified tops, presenting criteria for the determination of stratigraphic younging direction (Fig. ESM6F).

Intrusions

Several calc-alkaline, subvolcanic, feldspar ± quartz-porphyritic felsic intrusions occur within the stratigraphic succession (Fig. 2). This group includes porphyries with feldspar ± quartz phenocrysts set in a fine-grained, aphanitic groundmass, and phaneritic varieties where phenocrysts are set in a medium-grained ('granite-like') groundmass. For the latter, the porphyritic texture is the key field criteria for distinguishing these rocks from the GDG intrusions further east (Fig. 2). All the intrusions contain biotite as the main mafic mineral, and accessory titanite, apatite, and zircon.

Field relationships suggest that the steeply dipping porphyritic intrusion at Mellandammen (Mellandammen porphyry) is a dyke (Fig. 2). The Mellandammen porphyry contains up to 15 vol.% 1–4 mm embayed quartz phenocrysts, 20 vol.% 1–3 mm plagioclase phenocrysts, and 5–10 vol.% 1–3 mm K feldspar crystals, set in a fine-grained groundmass.

A feldspar porphyritic intrusion at the Bronäs Zn-Pb-Ag deposit ('Bronäs granodiorite', Figs. 2, 4A, ESM7) shows sharp, chilled, intrusive margins against Zn-Pb-Ag mineralization in drill core. The intrusion exhibits white plagioclase phenocrysts set in a medium-grained groundmass of microcline, quartz, and biotite. An anastomosing tabular form of this intrusive body and an orientation sub-parallel to adjacent volcanic interbeds in the limestone suggest that it is a sill. Despite bordering the main massive sulfide lens at Bronäs (Fig. 4A-B), the Bronäs granodiorite is only weakly sericite-altered and is not mineralized (Fig. ESM8D-E).

The largest feldspar + quartz-porphyritic intrusions occur west of the Sala limestone, in the stratigraphic hanging wall (Fig. 2). An evenly porphyritic dacite with 40 vol.% euhedral 1–5 mm plagioclase and 10 vol.% 1–4 mm blue-grey, embayed quartz phenocrysts (Långforsen porphyry) occurs near Lake Långforsen (Fig. 2). It contains enclaves of mafic rock, and owing to its crystal abundance is locally granodiorite-like in appearance. Contacts have not been observed. The Långforsen porphyry is apparently connected with another porphyry with chilled intrusive contacts NE of the Sala deformation zone, here termed the Stråbruken porphyry (Figs. 2, ESM8B), although the latter differs in composition and a higher phenocryst content. The Stråbruken porphyry contains up to 50 vol.% 1–5 mm plagioclase and 20 vol.% 1–5 mm quartz phenocrysts set in biotite-rich groundmass (Fig. ESM8B). This unit was dated at 1892 + 5/ − 4 Ma by Stephens et al. (2009).

A 10-m-wide, NNW-trending feldspar porphyritic dyke occurs in the Hyttskogen deformation zone (Stampers porphyry, Fig. 2). The phenocryst population is composed of 25 vol.% plagioclase and 15 vol.%. K feldspar, set in fine-grained, quartzofeldspathic groundmass. Finally, a feldspar porphyritic intrusion with 30 vol.% 1–2 mm plagioclaste

phenocrysts and 5 vol.% 1–2 quartz phenocrysts occurs in the northwest part of the study area (Sommarhagen porphyry, Fig. 2), but was not sampled for the current study. Ripa et al. (2002) described a peperitic margin towards adjacent volcaniclastic rocks, indicating emplacement prior to lithification of the latter (cf.McPhie 1993).

The eastern extent of the Sala limestone is controlled by a discordant contact with the Sala granite (Fig. 2), the westernmost pluton of the GDG unit east of Sala. Based on exposures in the exploration drill cores, the contact is intrusive and dips moderately westwards, truncating the Sala limestone and obscuring its stratigraphic lower contact. The granite has an average grain size of 3 mm dominated by oligoclase (33 vol.%), microcline (29 vol.%), quartz (35 vol.%), and biotite (2–3 vol.%, Fig. ESM8C). Subordinate aplite has been observed locally in drill core. The western contact against the dolomitic marble is sharp and displays a 1-m-thick, finer grained chilled margin. Schists consisting of biotite, chlorite, serpentine, and local amphibole occur at the contact, ranging in thickness from 10 cm to several meters. Marble less than 3 m from the granite contact exhibits coarsening to 2 mm.

With the exception of weak sericitization, weak epidote alteration of feldspar crystals, and metamorphic recrystallization (Fig. ESM8D-E), all the intrusions described above are virtually unaltered. However, oxide-coating and clay alteration is locally observed adjacent to faults and fractures near the surface. Detailed lithogeochemical characteristics of igneous rocks in the entire Sala inlier are the subject of a separate communication (Jansson et al. in prep). A subset of samples from least-altered intrusions in the Sala area is presented in ESM3 and Fig. ESM9A-C.

A sub-alkaline, granitic composition is confirmed by the total alkali vs. SiO_2 diagram of Middlemost (1994) for the Sala granite and the Mellandammen porphyry, whereas the other intrusions have compositions corresponding to granodiorite (Fig. ESM9A). A calc-alkaline affinity for all intrusions is suggested by the AFM diagram of Irvine and Baragar (1971) (Fig. ESM9B). In the alumina saturation diagram of Barton and Young (2002), most samples plot as weakly peraluminous but straddling the boundary to metaluminous compositions (Fig. ESM9C).

The age relationship between the numerous GDG and porphyritic intrusions is not fully clear due to few observed cross-cutting relationships. The Bronäs granodiorite is interpreted to be cross-cut by the Sala granite based on the fact that it is lacking in the Sala granite (Fig. 4A-B). Similarly, a NE branch of the Stråbruket porphyry is truncated by the Sala granite (Fig. 2).

Metamorphosed mafic intrusive rocks occur in the western and northern part of the field area, but have been studied to provide regional context. Field exposures are rich in calcic clinoamphibole, chlorite, epidote, and plagioclase

and commonly contain a fine pyrrhotite dissemination. These intrusions exhibit metamorphic recrystallization and an overprint by tectonic fabrics, distinguishing them from younger dolerite dykes in the area, which cross-cut deformed and metamorphosed rocks (Fig. 2).

Mineralization

Sphalerite and galena are the main ore minerals at both Sala mine and Bronäs, and have historically formed the basis for a division between sphalerite-rich and galena-rich ore bodies (Figs. 3A-B, 4A-B). Associated opaque minerals observed in the sample set of the current study include pyrite (porphyroblasts), magnetite, boulangerite, geocronite, freibergite, and rare diaphorite and jamesonite. Contacts between dolomite marble and massive sulfide mineralization are commonly razor sharp, with dolomite marble clasts occurring in a ductile-deformed sulfide matrix (Fig. ESM10A). Mapping, logging, inspection of hand specimens, and optic microscopy show that the ores are accompanied by a gangue rich in clinoamphibole, phlogopite, chlorite, serpentine, talc, calcite, clinozoisite, clinopyroxene (Fig. ESM10B), barite (Fig. ESM10C), and more rarely garnet (Fig. ESM10D) or tourmaline. The ore minerals and gangue generally exhibit lepidoblastic to granoblastic textures in thin section. In the following section, emphasis will be placed on documenting key textural relationship between ore minerals and the anhydrous and hydrous skarns occurring with the ore.

Anhydrous skarns

Clinopyroxene. Clinopyroxene is by far the predominant anhydrous skarn mineral in the Sala area and exhibits a strong spatial correlation with Zn-Pb-Ag mineralization, occurring as several centimeter-sized crystals in massive sulfide mineralization from Sala mine (Figs. 5A, ESM10B), and as bladed to granoblastic aggregates in 10–100 cm scale skarn zones at the contact between dolomite marble and massive sulfides (Fig. 5B-C). Zones of massive clinopyroxene are very rare further away from massive sulfide mineralization, clinopyroxene being completely absent in regional dolomite marble in Sala. There are for example no known occurrences of clinopyroxene in the dolomite marble in the currently accessible historic underground drifts in Sala mine (e.g. Figure 3A), despite direct proximity to several underground workings where clinopyroxene-bearing ore bodies were mined out.

Where seen in drill core from near Sala mine and Bronäs, clinopyroxene is generally highly volumetrically subordinate compared to massive sulfides, but also to paragenetically later hydrous skarn minerals, which will be described below in a separate section. An exception occurs in the Glasgruvan deposit (Fig. 2), where several meter thick zones of massive, monominerallic clinopyroxene occur in sharp contact with dolomitic marble, and form a host to sphalerite-rich massive sulfide mineralization that was mined at this deposit (Fig. 5C-E).

Electron microprobe analyses (EPMA) and backscatter electron imaging (BSE) reveal complex zonation patterns in gangue clinopyroxene crystals (Fig. 5A), reflecting variable contents of Fe, Mg, and Mn (ESM4). Oscillatory or complex mosaic-like patchy zonation patterns are common, e.g. zoning defined by early, complexly zoned clinopyroxene ($Di_{66.2}Hd_{28.7}Jhn_{5.1}$-$Di_{87.9}Hd_{9.6}Jhn_{2.5}$), truncated by later ferroan diopside of the composition $Di_{77.6}Hd_{19.4}Jhn_{3.0}$, in turn surrounded by an outer rim of clinopyroxene of the composition $Di_{67.0}Hd_{29.3}Jhn_{3.7}$ in contact with massive sphalerite and galena mineralization (Fig. 5A).

Granoblastic skarns occurring marginal to and hosting sulfide mineralization at Glasgruvan similarly exhibit a complex growth history. Granoblastic aggregates of early fine-grained, barren clinopyroxene exhibit substantial compositional zonation, ranging from $Di_{69.2}Hd_{26.4}Jhn_{4.5}$ to $Di_{99.4}Jhn_{0.6}$ (Fig. 5C). Optical microscopy reveals that the sphalerite-rich sulfide mineralization is spatially associated with a younger generation of coarser-grained, blocky euhedral clinopyroxene crystals, occurring in veins cross-cutting and replacing the granoblastic skarns (Fig. 5D). The rim of ferroan diopside that is in contact with sphalerite is more Mn-rich clinopyroxene than the core, which is of diopside composition (Fig. 5E). Sulfide inclusions are lacking in all observed clinopyroxene varieties. Instead, sulfides occur interstitial to clinopyroxene crystals or in veins cross-cutting them (Fig. 5B), commonly associated with paragenetically later calcite (Fig. 5D) and hydrous silicates (Fig. 5A-F).

The granoblastic and bladed clinopyroxene overlap compositionally at < 20 mol.% hedenbergite and < 5 mol.% johannsenite component. In contrast, euhedral clinopyroxene associated with massive sulfides (Fig. 5A and 5E) are generally more Fe- and Mn-rich, and show better compositional overlap with the compositional field of Zn skarns globally in Meinert et al. (2005) (Fig. ESM11).

Garnet. Monominerallic skarns of garnet are not known from the Sala area, and the mineral garnet is altogether rare in the studied skarns. It was only observed in two samples— both of massive sulfides—occurring as two texturally distinct types; (1) perfectly euhedral crystals, ranging in size from 1 to 5 mm and evenly distributed in the sphalerite-galena matrix in ore from Sala mine (Fig. 6A-B), and (2) xenoblastic crystals associated with K feldspar bearing sphalerite-galena mineralization from Bronäs (Fig. 6E-G). The euhedral garnet is black in hand specimen but has an orange tint in a 30-µm thin section, where they are anisotropic, sector-zoned and have inclusion-rich cores and inclusion-poor rims (Fig. 6A). Inclusion species identified
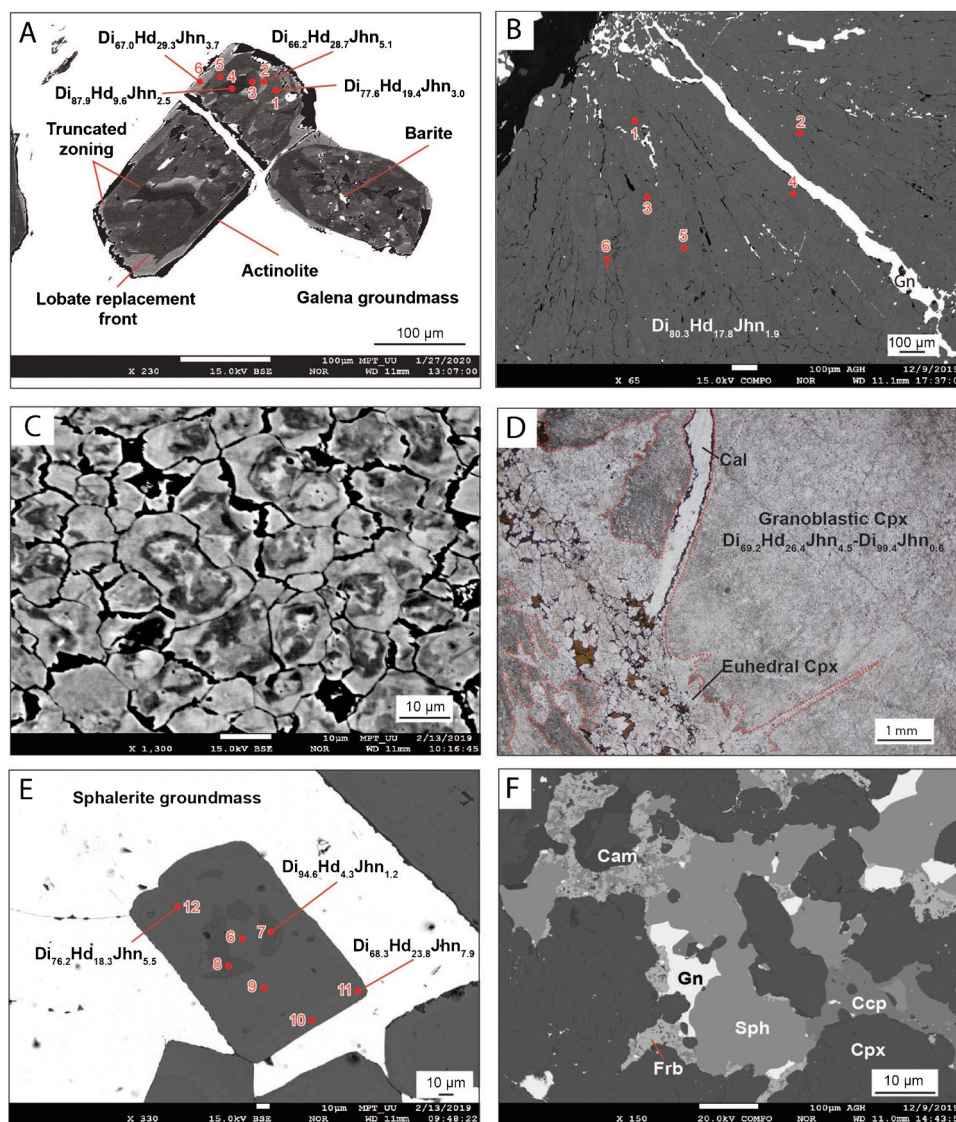
Fig. 5 Clinopyroxene-bearing skarns in the Sala area. Numbered points show the position of spot analyses in ESM4. (**A**) Euhedral crystal of clinopyroxene with an actinolite rim in massive galena (light). BSE contrast is maximized to highlight a complex internal zonation in the clinopyroxene crystal. Sample M3908, EPMA A4. (**B**) Bladed clinopyroxene skarn with galena along cross-cutting veins and interstitial to clinopyroxene crystals. Sample BRO55E11-49.5 from Bronäs, EPMA CPX1. (**C**) BSE view showing massive, fine-grained, granoblastic skarn consisting entirely of complexly zoned diopside-ferroan diopside crystals with turbid cores. Core clinopyroxene is heterogeneous but commonly includes close to end-member diopside, whereas later overgrowth clinopyroxene is more homogeneous and more Fe- and Mn-rich ferroan diopside. Sample SAA112-94.9 from Glasgruvan. (**D**) Transmitted light view, showing granoblastic clinopyroxene in 'C' overprinted by a younger generation of coarser-grained clinopyroxene, sphalerite, and locally calcite. Sample SAA112-94.9. (**E**) Close-up of later euhedral clinopyroxene in 'D', showing an internal zonation from more diopside-rich clinopyroxene in the center to johannsenite-rich ferroan diopside at the rim towards sphalerite. (**F**) Association of sphalerite, galena, chalcopyrite, and freibergite interstitial to clinopyroxene, which is altered to calcic clinoamphibole. Bronäs BRO55E11-49.5. Abbreviations; Cam: calcic clinoamphibole, Ccp: chalcopyrite, Cpx: clinopyroxene, Cal: calcite, Di: diopside, Frb: freibergite, Gn: galena, Hd: hedenbergite, Jhn: Johannsenite, Sph: sphalerite

or analyzed with EPMA are ferroan diopside, galena, sphalerite, barite, pyrite and lesser boulangerite, K feldspar, and albite. Included clinopyroxene crystals display alteration to amphibole and sulfides, and clinopyroxene and garnet are commonly separated by a clinoamphibole rim. Sulfide inclusions are subordinate (Fig. 6B, E).

The analyzed euhedral garnets (Fig. 6B) belong to the andradite-grossular series, with dominance of andradite, ranging between 33.2 and 75.6 mol% (ESM4). The grossular component locally exceeds andradite but does not exceed 57.42 mol % in the analyzed sample (Fig. 6C). The pyralspite series garnet component is ≤ 10 mol% in and is

Fig. 6 Garnet from Sala mine and Bronäs. Numbered points show the position of spot analyses in ESM4. (**A**) Crossed polarizer view of garnet of euhedral garnet in a sphalerite-galena (SPH-GN) matrix in sample M3908, showing sector zoning and inclusion-rich core. (**B**) BSE view of sector zoned garnet in M3908, showing an andradite (ADR) rim, actinolite (ACT) at the margins, and the position of EPMA spot and traverse analyses. (**C**) End-member components along the traverse in 'B', calculated from data in ESM4. (**D**) Close of faint, oscillatory zoning along the outer rim of garnet as in 'D'. Also shown are inclusions of clinopyroxene (CPX) and calcite (CAL). (**E**) BSE view of complexly zoned, xenoblastic garnet with a pyrite (PY) inclusions and a lobe of clinopyroxene. Smaller garnet crystals near edges of photo are rich in inclusions of K feldspar (KFS), which also forms a matrix to the garnet crystals along with clinopyroxene. Sample BRO8A-17.8 (Fig. 2). (**F**) Compositional map of alumina distribution, (**G**) compositional map iron of iron distribution. See ESM4 for data and mapping conditions
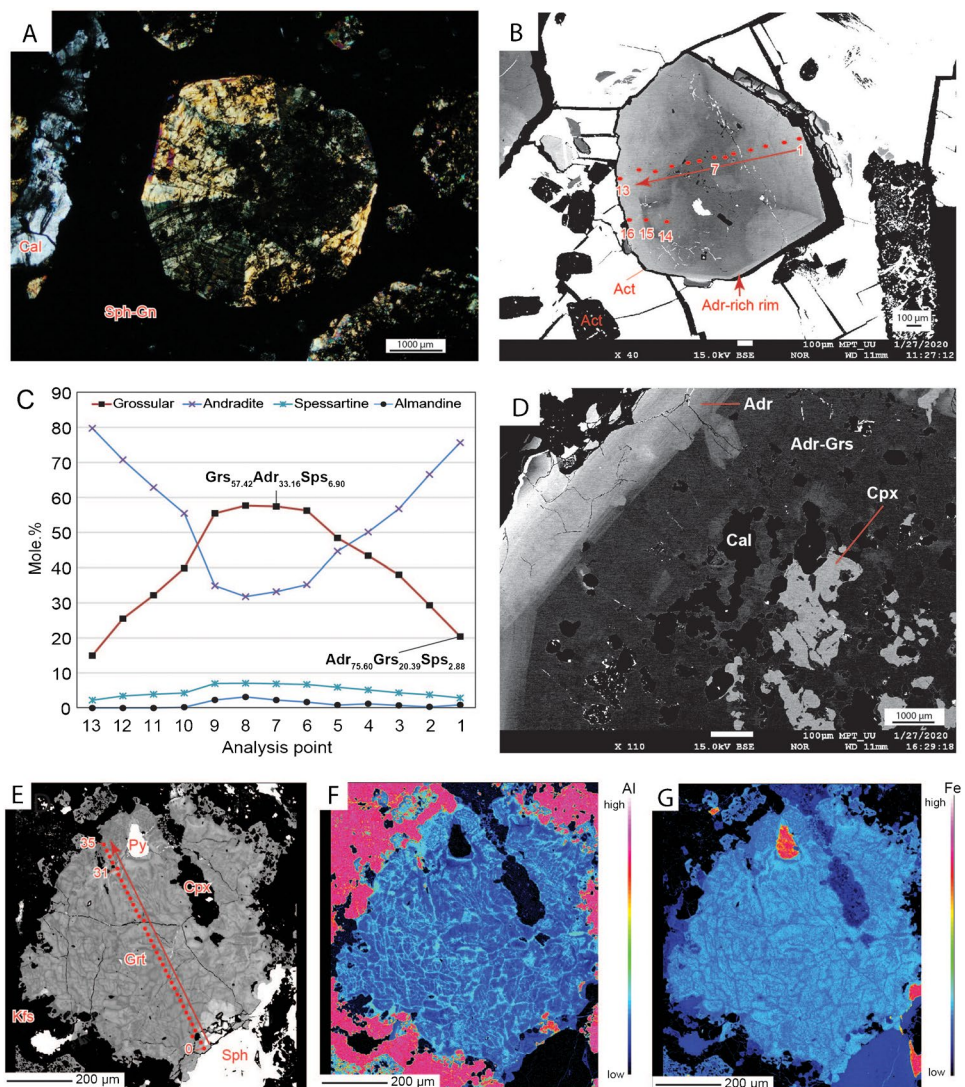
dominated by spessartine (≤ 7 mol.%) followed by almandine (≤ 3 mol.%), then pyrope (≤ 1 mol.%). The uvavorite content is insignificant. The sector zoning under crossed polarizer is observed in BSE view to be associated with a compositional difference, expressed by a higher grossular component at interfaces between different sectors (Fig. 6B). The core is of andraditic grossular composition, whereas the rim is andraditic (Fig. 6C). However, the internal core-to-rim zonation is complex and variable in different orientations in a single crystal (Fig. 6B). Along some orientations, a gradational zonation of increasing andradite and decreasing grossular, almandine, and spessartine is observed from core to rim (Fig. 6C). Along other orientations, garnet of more grossularitic composition extends to the outer part of the crystal, where it exhibits a sharp transition to an outer rim of andradite garnet (Fig. 6B and 6D).

Some garnet crystals show oscillatory zoning parallel to crystal faces, defined by optical interference colors under crossed polarizers (Fig. 6A), yet oscillatory zoning is commonly lacking or indistinct in BSE view (Fig. 6B). An exception is the outermost andradite-rich rims which exhibit vague oscillatory zoning in BSE images. (Fig. 6D).

The xenoblastic garnet occurs in sphalerite-galena mineralization with a gangue of K feldspar and clinopyroxene. Inclusions of K feldspar and pyrite occur particularly in smaller grains or near the margins of larger grains (Fig. 6E-G). The internal texture comprises a complex, mottled pattern in BSE images, wherein BSE pale domains are enveloped by a network of BSE dark domains with curved outlines (Fig. 6E). The lighter domains in BSE correlate with high iron content, whereas the dark domains reflect higher contents of aluminum (Fig. 6F-G). All spot analyses of garnet from Sala and Bronäs plot in the field of Zn skarn deposits of Meinert et al. (2005) (Fig. ESM12).

Hydrous gangue silicates

Sphalerite, galena, chalcopyrite, and sulphosalts do not occur as inclusions in any of the clinopyroxene varieties described above, and are highly subordinate as inclusions in garnet (Fig. 6B, E). Instead, the majority occurs interstitially or in veins (Fig. 5B), or associated with a hydrous gangue assemblage of phlogopite, chlorite, amphibole, serpentine, talc, calcite, and locally magnetite that are locally seen to have veined, overgrown, or replaced clinopyroxene and garnet (Figs. 5A, F, ESM13A). Vein networks and breccia infilling of these hydrous minerals are very common in the dolomite marble adjacent to massive sulfide mineralization in Sala mine (e.g. Figure 3A). In Sala mine, such vein networks and breccia infilling are seen to be gradational to semi-massive sulfide mineralization of the type seen in Fig. ESM10A when traced along strike, expressed by a gradational increase in base metal sulfides and a decrease in silicates.

The amphibole gangue is close to end-member tremolite at Mg/(Mg + Fe^{2+}) = 0.97–1.00 and low MnO (< 0.24 wt.%, ESM4). An exception is the actinolite replacing ferroan diopside in Fig. 5A, which has Mg/(Mg + Fe^{2+}) = 0.77–0.78 and a considerably higher MnO content (0.94–1.08). Chlorite which is another common hydrous gangue mineral has Mg/(Mg + Fe^{2+}) = 0.96 and Si^{IV} = 6.33–6.36, and classify as penninite in the nomenclature of Hey (1954)(ESM4). Magnetite associated with tremolite and chlorite has a close to end-member composition, containing 0.37 wt.% MgO and 0.29–0.38 wt.% MnO (ESM4). Serpentine and talc are both of Mg-rich composition, with less than 1.24 and 2.44 wt.% FeO, and less than 0.06 and 0.01 wt.% MnO, respectively (ESM4).

Phlogopite crystals are commonly perfectly euhedral (Fig. ESM13C) and exhibit alteration to chlorite. Analyzed crystals are characterized by low iron (Mg/(Mg + Fe) = 0.92–0.98)), low Mn (MnO = 0.12–0.15 wt.%), and 0.86–0.92 wt.% F. A considerably more F-rich (4.58 wt.%) variety was found in sphalerite-galena mineralization overprinting barite at Bronäs (Fig. ESM13B). This phlogopite contains 3.12 wt.% BaO, reflecting 10 mol % of the rare kinoshitalite component (Gnos and Armbruster 2000).

Sulfur isotope compositions

The δ^{34}S$_{V\text{-}CDT}$ values of sphalerite and galena from the Sala deposit range between − 0.94 and + 3.62‰ based on 21 analyses (ESM5, Fig. ESM14). The variations in δ^{34}S$_{V\text{-}CDT}$ value of sphalerite and pyrite from Sala mine exhibit a gradational yet somewhat irregular increase from south to north (Fig. ESM14), from δ^{34}S $_{V\text{-}CDT}$ = + 0.56 to + 1.57‰ in the southernmost part to δ^{34}S$_{V\text{-}CDT}$ = + 1.94 to + 3.25‰ in samples from drill core SAA12011 which intersect the downplunge continuation of the deposit 700 m further northwest

(Fig. ESM14, see Fig. 2 for location). This trend is supported by δ^{34}S$_{V\text{-}CDT}$ values in galena, and low δ^{34}S$_{V\text{-}CDT}$ values in geocronite in mineralization in the southernmost part of the mine (− 0.25 to − 0.06‰). It is however contradicted by high δ^{34}S$_{V\text{-}CDT}$ values in jamesonite (+ 3.33‰) and boulangerite (+ 2.43‰). However, the subordinate nature of these minerals in relation to sphalerite should be kept in mind, whereby sphalerite, pyrite, and galena better reflect the total sulfur budget of the deposit. An upwards increase in δ^{34}S$_{V\text{-}CDT}$ is indicated by a δ^{34}S$_{V\text{-}CDT}$ value + 4.17‰ in pyrite, but few samples from the upper part of the deposit preclude a firm statement regarding vertical zonation. This δ^{34}S$_{V\text{-}CDT}$ value is similar to pyrite porphyroblasts in barren dolomite marble from Tistbrottet (Fig. 2), which returned a δ^{34}S$_{V\text{-}CDT}$ of + 3.80‰.

δ^{34}S$_{V\text{-}CDT}$ values in sphalerite and galena from Glasgruvan are similar to those at Sala, whereas samples from Bronäs deposit yielded lighter δ^{34}S$_{V\text{-}CDT}$ values in the range − 1.07 to − 0.07‰ (Fig. ESM14). Pyrite from Bronäs returned an anomalously low value of − 5.22‰. Barite δ^{34}S$_{V\text{-}CDT}$ range between + 5.61 and + 7.17‰, which is considerably higher than sulfides replacing barite in the same sample.

Alteration

Discordant dolomitization fronts that overprint and texturally degrade stromatolites in calcite marble in the Kalkbacken area (Fig. 7A, see Fig. 2 for location) illustrate that dolomite is secondary and formed by replacement of calcitic, stromatolitic limestone (Ripa et al. 2002; Allen et al. 2003). The dolomite marble is of regional extent, ranges in color from grey to light-green (Fig. 7B), and generally carries < 15 vol.% silicates (calcic clinoamphibole, chlorite, serpentine, phlogopite) associated with calcite. Hence, unlike clinopyroxene and garnet, these minerals are not unique to ore gangue, but also constitute a regional metamorphic mineral association in the Sala area. Reaction skarns of these minerals, ranging in thickness from 1 to 10 cm, are common at the contacts between dolomite and interbeds of metavolcanic rocks throughout the region (Fig. 7C). Calcic clinoamphibole locally forms centimeter-sized radial crystal aggregates or streaks and patches in dolomitic marble. More locally, the dolomite marble has attained a white, bleached color (Fig. 7D), for example at Tistbrottet (Fig. 2) where it is exploited as industrial dolomite.

During mapping, zones exhibiting elevated magnetite, sulfides, and hydrous Mg silicates were observed within a few 100 m of the Zn-Pb-Ag deposits (Figs. 2, 7E-F). These zones of magnetite- and sulfide-enriched dolomite marble generally coincide with positive magnetic anomalies on the airborne geophysical map presented by Ripa et al. (2002) and unpublished legacy ground magnetic

Fig. 7 (**A**) Texturally destructive discordant dolomitization front (black-weathered) overprinting stromatolites in calcite marble at Kalkbacken (Fig. 2). Picture from Ripa et al. (2002). (**B**) Typical distal, grey dolomite marble in the Sala area. Sample LC20172023, (SWEREF 99TM, E: 586,907, N: 6,641,553). (**C**) Pyrite-bearing tremolite-phlogopite reaction skarn at contact between rhyolitic ash-siltstone and light dolomite marble at Tistbrottet (Fig. 2). (**D**) Highly pure, white dolomite marble from Tistbrottet (Fig. 2). (**E**) Typical patchy texture observed in magnetite- and sulfide-enriched dolomite marble. Dark patches mainly consist of serpentine (Srp) with lesser tremolite (Cam), magnetite (Mag), pyrrhotite (Po), calcite (Cal), sphalerite, and galena. Relict forsterite crystals are locally found. (**F**) Patches of tremolite (Cam), serpentine (Srp), chlorite (Chl) in grey magnetite- and sulfide-enriched dolomite marble
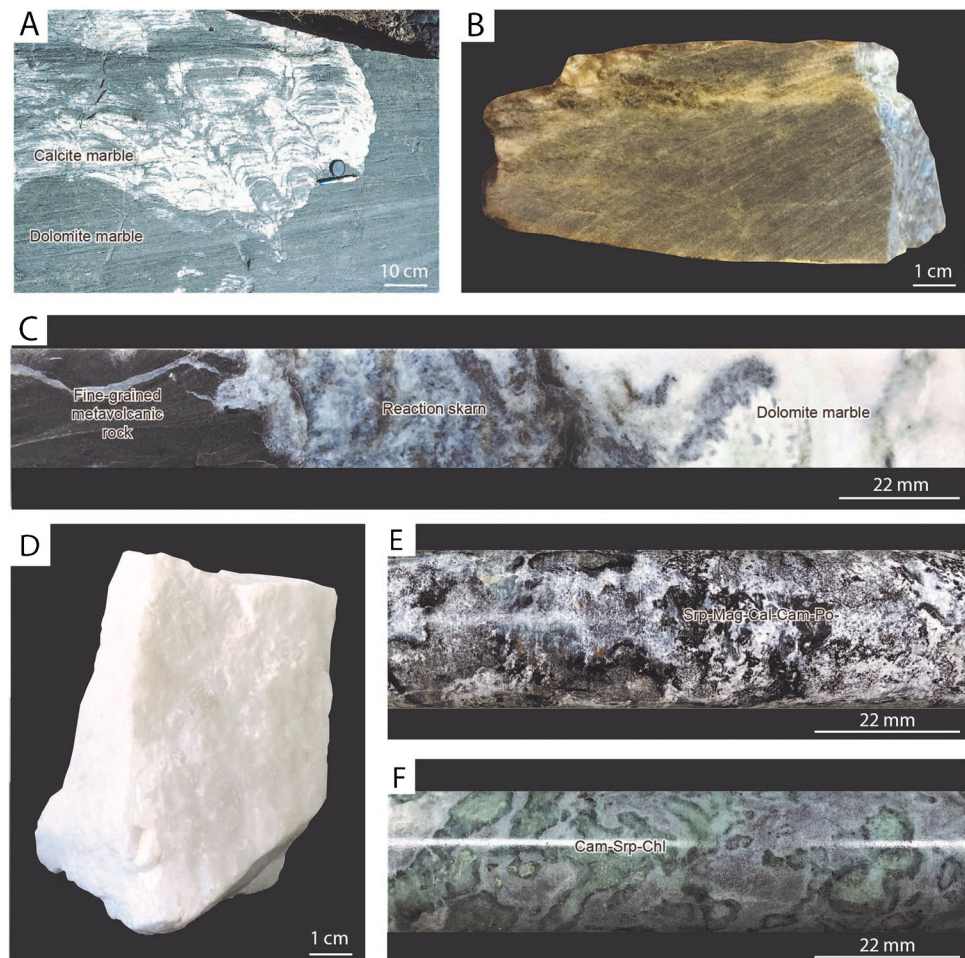
data belonging to Boliden Mineral AB. The zones of magnetite- and sulfide-enriched dolomite marble outline a complex branching geometry, ranging from concordant to metavolcanic interbeds, to discordant (Fig. 2). They essentially form alteration haloes around most known Zn-Pb-Ag deposits.

The Bronäs and Sala deposits are hosted by separate magnetite- and sulfide-enriched zones, and another prominent zone occurs between them (the Vattengruvan alteration zone). The Vattengruvan and Sala mine zones converge into a 300-m-wide zone of magnetite- and sulfide-enriched dolomite marble adjacent to the contact of the Sala granite, and then extends all the way to the southern contact of the marble (Fig. 2).

Yet another similar alteration zone can be defined adjacent to the Sala granite in the Gudmundstorp area in the northern part of the marble (Fig. 2). The relationship of the Gudmundstorp alteration zone to the ones in the south is unknown (Fig. 2).

Mineralogical zonation

Observed from drill hole SAA12011 (Fig. 2), mineralogical zonation from barren dolomite towards massive Zn-Pb-Ag mineralization includes an increasing sulfide content, and a somewhat irregular increase in the amount of calcic clinoamphibole, chlorite, serpentine, magnetite, and calcite (Fig. 8A-B). EPMA analyses reveal that dolomite and calcite in magnetite- and sulfide-enriched dolomite marble (Fig. 7E–F) are considerably richer in MnO than in barren dolomite marble from Tistbrottet (Fig. ESM15), but lower than in dolomite occurring directly adjacent to, or as clasts in, breccia-type sphalerite-dominated semi-massive sulfide as shown in Fig. 9A (ESM4). A positive linear correlation ($R^2 = 0.92$) can be defined between MnO_{Dol} and MnO_{Cal}, suggesting that dolomite is consistently 0.10 wt.% higher in MnO than calcite and that both increase from distal to proximal. The FeO content is higher in dolomite, although there is no systematic relation between FeO in dolomite and
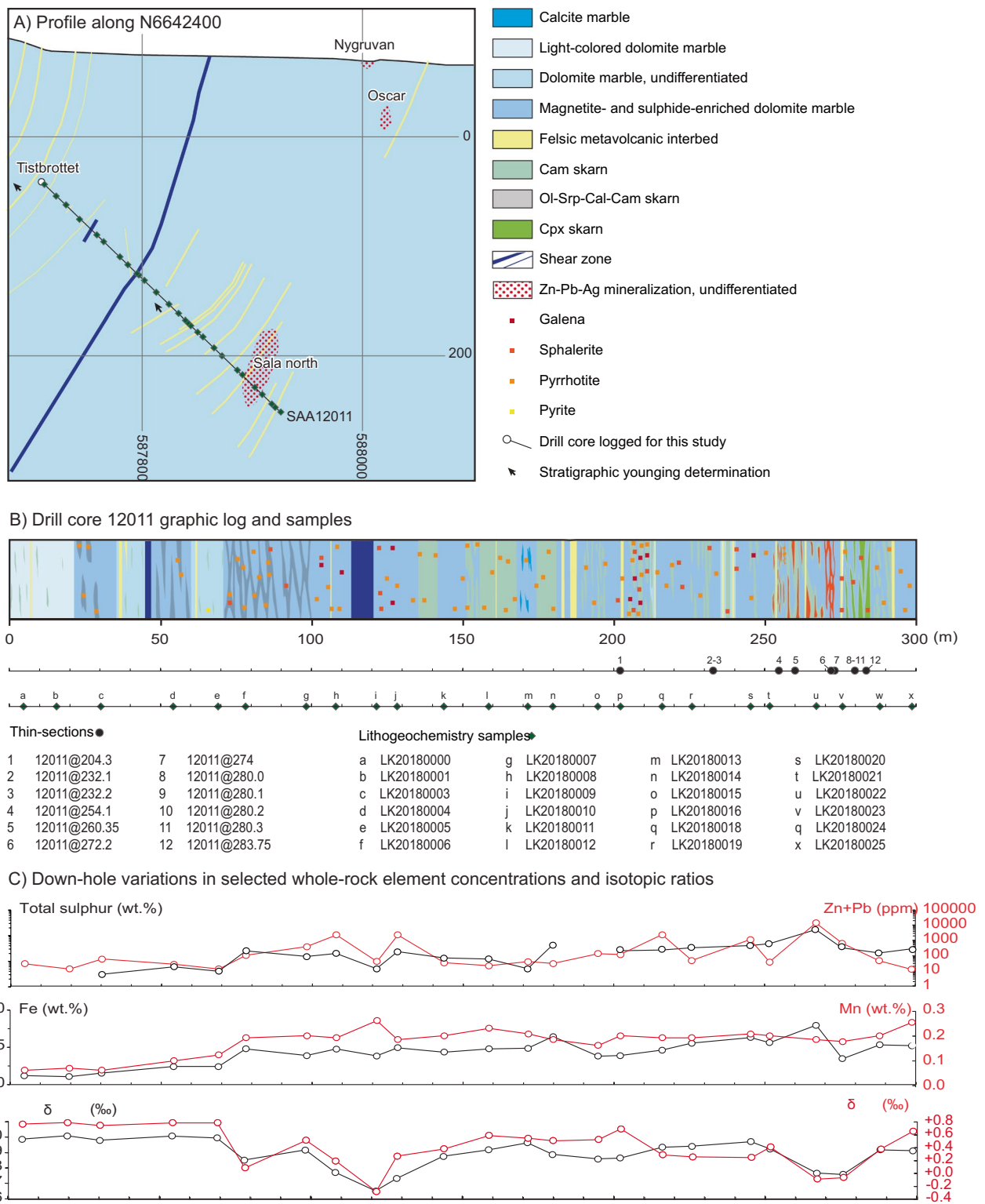
Fig. 8 (**A**) Schematic geological profile of the area east of Tistbrottet, showing the underground exploration drill hole SAA12011 (see Fig. 2 for location) intersecting a northern extension of the Sala deposit ('Sala north'). Dips of felsic metavolcanic interbeds are based on surface mapping and adjacent drill cores (not shown). Grid is SWEREF99TM. (**B**) Detailed graphic log showing lithological and mineralogical variation and sample distribution. (**C**) Selected elements from whole-rock lithogeochemical data (ESM2) from drill core SAA12011 (Fig. 2), plotted to visualize chemical variations from barren to mineralized marble. Also plotted are δ¹³C_V-PDB and δ¹⁸O_V-SMOW values (ESM5). Abbreviations: Cal: calcite, Cam: calcic clinoamphibole, Cpx: calcic clinopyroxene, Ol: olivine, Srp: serpentine

Fig. 9 Optical and BSE micrographs of magnetite- and sulfide-enriched dolomite marble. (**A**) Cross-polarized view of xenoblastic forsterite porphyroblast embedded in calcite in dolomite marble. (**B**) BSE image showing a forsterite crystal with calcite halo in dolomite marble (dolomite is not seen in picture), incompletely replaced by serpentine along veins. Note BSE-bright intergrowths of magnetite and pyrrhotite in serpentine. 12,011–280.2. (**C**) Cross-polarized view of hydrous association of tremolite, pyrrhotite and lesser galena overprinted by associations of calcite, serpentine, and chlorite. (**D**) Same view as 'C' under reflected light. Abbreviations: Cal: calcite, Mag: magnetite, Ol: olivine, Po: pyrrhotite, Srp: serpentine, Tr: tremolite
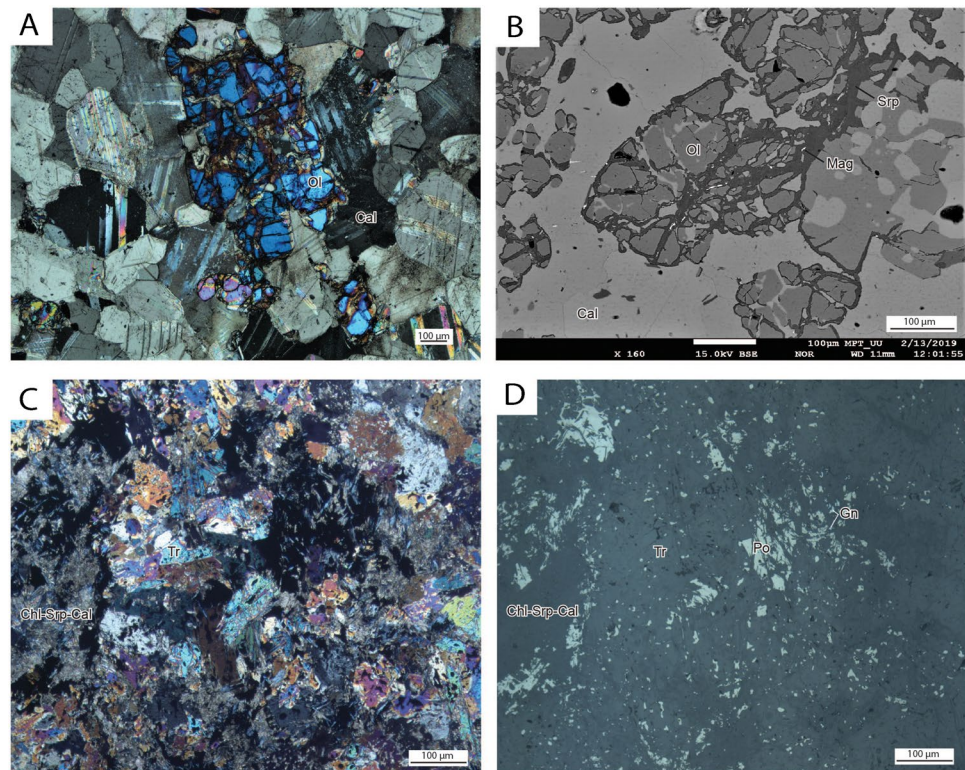
calcite (Fig. ESM15B). The FeO_{Dol} content in magnetite- and sulfide-enriched dolomite marble overlaps with barren dolomite marble, but is notably higher in massive Zn-Pb-Ag mineralization (Fig. ESM15B).

Pyrrhotite-galena-magnetite-black serpentine-calcite is a common mineral association in the spotted marble shown in Fig. 7E, and in SAA12011 this variety is common 150–200 m away from mineralization (Fig. 8B). Optical microscopy reveals that the dark spots contain relict olivine porphyroblasts with calcite haloes (Fig. 9A–B). Intact olivine crystals that were analyzed by EPMA ($n = 3$) were all of forsterite composition ($Fo_{94}Fay_5$-$Fo_{96}Fay_4$) with a negligible MnO content (ESM4).

The content of patchy calcic clinoamphibole increases towards mineralization (Figs. 8, 9C–D). EPMA analyses show that the calcic clinoamphibole is close to end-member tremolite at $Ca/(Ca + Mg) > 0.96$ (ESM4). The $(Mn + Fe^{2+})/Mg$ ratio in amphibole is similar to that in dolomite from the same sample except for amphibole gangue in Zn-Pb-Ag mineralization (Fig. ESM16A). Analogous to the dolomite results, this translates into an increase in the FeO and MnO content in amphibole from distal to proximal relative to Zn-Pb-Ag mineralization (Fig. ESM16B). Tremolite from the light-colored dolomite marble at Tistbrottet exhibits a somewhat lower Si content and a slightly higher Al_2O_3 content than the other types (ESM4).

Magnetite and pyrrhotite are associated with black serpentine, dark-green chlorite and calcite, which are observed

to replace forsterite (Fig. 9B), and locally also tremolite (Fig. 9C–D). The chlorite in marble + sulfide-enriched dolomite marble and Zn-Pb-Ag mineralization is of penninite composition, contrasting with chlorite in barren dolomite marble from Tistbrottet, which at $Mg/(Mg + Fe^{2+}) = 0.98$ and $Si^{IV} = 5.87$ is clinochlore in the classification of Hey (1954). The magnetite contains 2.18 wt.% MgO and 1.06 wt.% MnO (ESM4).

Dolomite whole-rock lithogeochemistry

The mineralogy and mineral chemistry suggest that alteration and mineralization at Sala is associated with formation of minerals carrying elevated Fe and Mn in relation to the dolomite precursor. Whole-rock data on the distribution of these elements in marble (ESM2) can thus be used for further characterizing the alteration zones.

The whole-rock Mn content in dolomite marble shows a somewhat polymodal distribution in a probability plot (Fig. 10A), defined by inflection points at 0.07 and 0.18 wt.%, which are here used to divide samples into low, moderate, and high Mn groups. A similar tendency towards a polymodal distribution is exhibited by Fe, with an inflection point at 0.04 wt.% (Fig. 10B). The Mn contents of the low to moderate Mn groups correspond well to regional, unaltered marble in Bergslagen as suggested by Allen et al. (2003). Whole-rock Mn exhibits a positive correlation with Fe ($R^2 = 0.79$, Fig. 10C). With the exception of light-colored

Fig. 10 Selected elements from whole-rock lithogeochemical data in ESM2, color-coded according to Mn content (10 equal ranges). (**A**) Probably plot of whole-rock Mn content (ESM2), showing inflection points at 0.07 and 0.19 wt.%; the basis for division into low, moderate, and high with regard to Mn enrichment. (**B**) Probability plot of total iron content expressed as Fe. (**C**) Total Fe vs Mn (wt.%), exhibiting a positive correlation at $R^2 = 0.78$. (**D**) Probability plot of sulfur. Particularly in the low Mn group, sulfur was generally below the lower detection limit
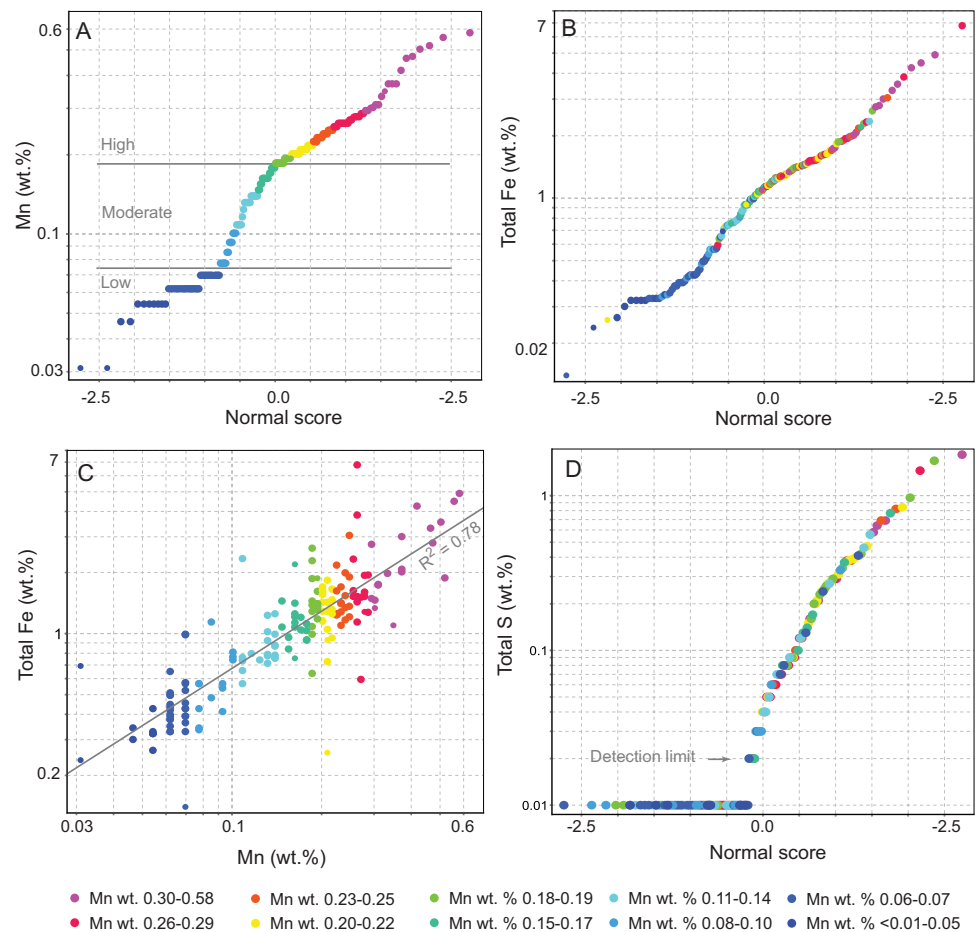
dolomite marble from Tistbrottet, the average Fe:Mn ratio suggested by the regression line (6.75) is higher than Fe:Mn values measured in the mineral dolomite (1.51–2.3 based on data in ESM4). This is most likely related to the presence of Fe-bearing silicates, magnetite and sulfides in the Mn-rich dolomite marble. Whole-rock total sulfur content varies a lot in the different groups defined using Mn content, but in general tends to be below the 0.02 wt.% detection limit in low Mn dolomite marble, whereas it is elevated in the Mn-rich marble (Fig. 10D).

Both Fe and Mn increase from barren dolomite marble to magnetite- and sulfide-enriched dolomite marble to mineralization in SAA12011 (Fig. 8C). The Fe + Mn-rich zone is here also characterized by a general enrichment in base metals, sulfur (Fig. 8C), and more sporadic anomalies in arsenic (ESM2) relative to barren dolomite marble at the start of the drill core. On a larger scale, The Mn content in dolomite marble increases from north to south and towards Zn-Pb-Ag mineralization in the southern part of the Sala area, with high Mn samples outlining a broad alteration halo around the area hosting the studied deposits (Fig. 11A). This Mn enrichment halo is cryptic in the sense that it has a greater extent than the mapped distribution of magnetite- and

sulfide-enriched dolomite marble. Most likely, Mn here occurs as a lattice bound substitution in dolomite and there is no visible evidence for its presence in hand specimen.

The Fe_2O_3:FeO ratio shows a general increase from west to east, and samples with Fe_2O_3:FeO > 1.2 show a generally good coincidence with mapped zones of magnetite- and sulfide-enriched dolomite marble (Fig. 11B). Magnetite is by far the most commonly observed mineral with essential Fe_2O_3-content in the alteration system, with andradite being a rare mineral. Hence, the pattern defined by Fe_2O_3:FeO distribution largely reflects the distribution of magnetite, being most elevated in magnetite- and sulfide-enriched dolomite marble near the Zn-Pb-Ag deposits at Sala, Bronäs, and Glasgruvan. Some samples exhibit higher whole-rock Fe_2O_3:FeO ratios, exceeding the theoretical end-member Fe_2O_3:FeO ratio of magnetite (2.21), which indicates that there are other ferric minerals in these samples. The highest measured Fe_2O_3:FeO ratio (8.83) was measured in sample LC20180101, which was collected only 5 m from the sampling site of the garnet-bearing thin-section BRO8A-17.8 (Fig. 2, Fig. 6E–G). Elevated Fe_2O_3:FeO due to secondary alteration of magnetite to hematite is unlikely since care was taken to not sample

Fig. 11 Whole-rock lithogeochemical data from the southern part of the Sala area (N = 157) plotted on a bedrock geological map (see Fig. 2 for legend). (**A**) Mn, (**B**) Fe_2O_3/FeO. The Mn variation can be used to outline a broad Mn halo west of Sala mine. Samples with elevated Fe_2O_3/FeO are more restricted to areas showing elevated contents of magnetite and more rarely andradite adjacent to Zn-Pb-Ag mineralization. The colour and size ranges of symbols were then defined using the 10 equal ranges algorithm in ioGAS™
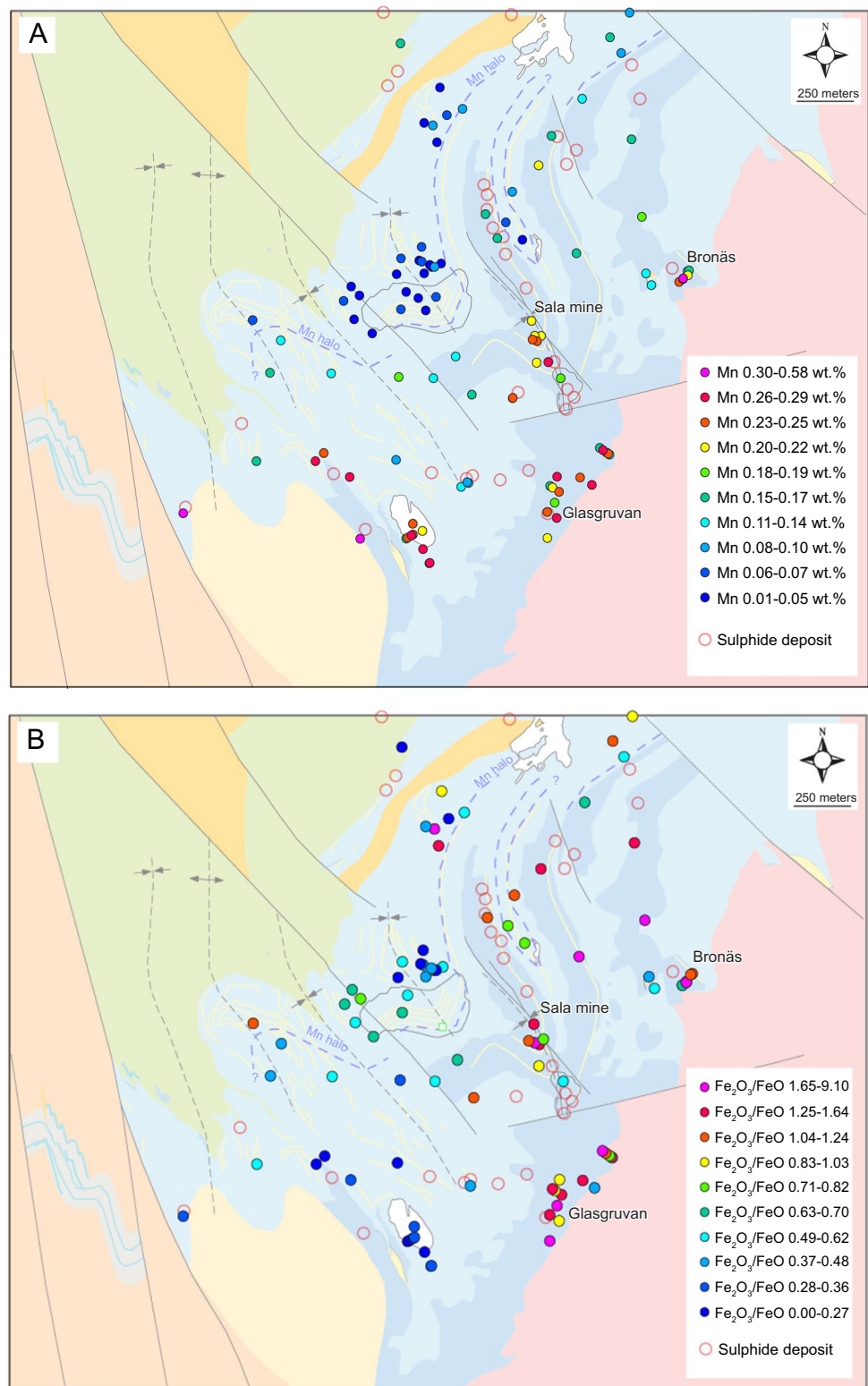
oxidized and weathered materials, and hematite alteration of magnetite was not observed in any of the thin sections. Hematite may however account for some outliers away from sulfide deposits.

Carbon and oxygen isotopes

Negative anomalies in $\delta^{18}O_{V\text{-}SMOW}$ and $\delta^{13}C_{V\text{-}PDB}$ occur in the magnetite- and sulfide-rich dolomite marble in

SAA12011, centered on a shear zone and base metal sulfide mineralization (Fig. 8C). Plotting Mn vs. $\delta^{13}C_{V-PDB}$ and $\delta^{18}O_{V-SMOW}$ illustrates that the Mn-rich samples also tend to be isotopically lighter than the low-moderate Mn samples, albeit there is substantial spread, in particular for $\delta^{18}O_{V-SMOW}$ (Fig. 12A–B). Two samples of texturally well-preserved and chemically pure calcite and dolomite marble from the Kalkbacken area from Allen et al. (2003) are characterized by high $\delta^{13}C_{V-PDB}$ (+0.32 and +1.08‰), high $\delta^{18}O_{V-SMOW}$ (+19.63 and +20.85‰), low Mn (0.03 and

0.05 wt.%), and low SiO_2 (1.62 and 0.74 wt.%) and can be regarded as least-altered samples.

There is no clear relation between Fe_2O_3/FeO and $\delta^{13}C_{V-PDB}$ and $\delta^{18}O_{V-SMOW}$ (Fig. 12C–D), except for that the two samples with highest Fe_2O_3/FeO are also the ones with the lowest $\delta^{13}C_{V-PDB}$. These two samples are also among those returning the lowest $\delta^{18}O_{V-SMOW}$ values (Fig. 12D). Samples with elevated SiO_2 show lighter $\delta^{13}C_{V-PDB}$, although with substantial scatter (Fig. 12E). There is no clear relationship with Mn content; even relatively Mn-poor

Fig. 12 Relationship between Mn content and $\delta^{13}C_{V-PDB}$ (**A**) and $\delta^{18}O_{V-SMOW}$ (**B**), showing that Mn-enriched samples tend to be enriched in the lighter isotopes in relation to least-altered calcite and dolomite marble samples from the Kalkbacken area (Fig. 2). A similar trend is not as clear for samples with elevated Fe_2O_3/FeO (**C–D**), except for a few samples at extreme values. Samples with low $\delta^{13}C_{V-PDB}$ also tend to be enriched in SiO_2 (**E**). (**F**) $\delta^{13}C_{V-PDB}$ vs. $\delta^{18}O_{V-SMOW}$ plot, also showing the global averages for Orosirian dolomite and calcite marble are averages calculated based on the Precambrian Marine Carbonate Isotope Database (PMCID) of Shields and Veizer (2002). Isotopic shifts due to batch volatilization (dashed black lines) and Rayleigh volatilization (black lines) are modelled using fluid-rock fractionation factors (α) for siliceous dolomite from Valley (1986). Shifts due to infiltration of a magmatic-hydrothermal fluid at $\delta^{18}O_{V-SMOW}=6.3$ and $\delta^{13}C_{V-PDB}=-5$ (Taylor Jr 1986) at different T and XCO_2 are modelled using the approach of Bowman et al. (1985)

samples can exhibit low $\delta^{13}C_{V-PDB}$ and elevated SiO_2. However, at a given SiO_2 content, more Mn-enriched samples tend to return lower $\delta^{13}C_{V-PDB}$.

The least-altered samples are characterized by $\delta^{18}O_{V-SMOW}$ and $\delta^{13}C_{V-PDB}$ values close to those of average Orosirian calcite and dolomite marble (Fig. 12F), calculated from the Precambrian Marine Carbonate Isotope Database (PMCID) of Shields and Veizer (2002). The remaining samples define arrays trending towards lighter values. At a given $\delta^{18}O_{V-SMOW}$ value, the Mn-enriched samples generally exhibit lower $\delta^{13}C_{V-PDB}$, as expected from Fig. 12A. Hence, calcite marble samples and moderately Mn-enriched samples (up to 0.19 wt.% MnO) define a trend towards $\delta^{13}C_{V-PDB} = -1‰$ and $\delta^{18}O_{V-SMOW} = +11‰$, whereas the most Mn-rich (> 0.19 wt.%) samples trend towards significantly lower $\delta^{13}C_{V-PDB}$ values of -2 to $-4‰$ within the same $\delta^{18}O_{V-SMOW}$ range (Fig. 12F).

Calcite gangue and calcite occurring in veins that postdate ductile deformation commonly have similar $\delta^{18}O_{V-SMOW}$ values as immediately adjacent marble, but tend to exhibit lower $\delta^{13}C_{V-PDB}$ values. Most of these calcite samples plot along the modelled pathways for metamorphic decarbonation reactions for batch and Rayleigh decarbonation, calculated using parameters for siliceous dolomite (Valley 1986) and the $\delta^{13}C_{V-PDB}$ and $\delta^{18}O_{V-SMOW}$ of the least-altered dolomite marble as starting values. However, one sample (SALA-SB) shows a significantly lower $\delta^{18}O_{V-SMOW}$ value (+ 11.96‰).

In contrast, the majority of marble samples consistently plot to the left of the modelled pathways for metamorphic decarbonation reactions between carbonates and silicates (Fig. 12F). The array defined by these samples exhibit better overlap with expected pathways for interaction with an isotopically lighter fluid at different XCO_2, calculated using the approach of Bowman et al. (1985). The pathways have been modelled based on a hypothetical magmatic-hydrothermal fluid of $\delta^{18}O_{V-SMOW} = 6.3$ and $\delta^{13}C_{V-PDB} = -5$ (Taylor Jr 1986) at $T = 300–500$ °C and $XCO_2 = 0.1–0.5$.

Discussion

Ore genetic inferences from geological mapping

The majority of Zn-Pb-Ag deposits occur in the central parts of extensive zones of magnetite- and sulfide-enriched dolomite marble, wherein there are also high contents of hydrous silicates (serpentine, tremolite, chlorite). These zones exhibit complex branching geometries, partly following stratigraphic contacts of felsic interbeds (e.g. Figure 2), and partly following discordant deformation zones cross-cutting the stratigraphy (Fig. 3A–B). Distal to deformation zones in the area between Sala mine, Vattengruvan and Bronäs (Fig. 2), the distribution of magnetite- and sulfide-enriched dolomite marble is largely stratabound to specific stratigraphic intervals within the Sala limestone. Proximal to the SSZ in Sala mine, the several different branches of stratabound magnetite- and sulfide-enriched dolomite marble converge into a single, discordant zone, which can be traced southwards across Glasgruvan (Fig. 2).

F_1 folding of the stratabound zones of magnetite- and sulfide-enriched dolomite marble (Fig. 2) as well as the outer contact of the distal, more cryptic halo of Mn enrichment (Fig. 11A) indicates that alteration and associated mineralization formed prior to D_1 deformation at c. 1.87 Ga (Stephens and Jansson 2020). This explains why mineralization at Sala mine plunges sub-parallel to F_1 fold axes, and is folded by F_2 (Fig. 3A–B). It is furthermore consistent with mineralized and altered rocks being cross-cut by unaltered to weakly altered early intrusions, such as the Bronäs granodiorite (Fig. 4A–B), which in turn are cross-cut by the Sala granite, dated at 1891 ± 6 Ma by Stephens et al. (2009) (Fig. 2). Similarly, in the Gudmundstorp alteration zone in the northern part of the area, the Stråbruken porphyry—dated at $1892 + 5/\text{-}4$ Ma by Stephens et al. (2009)—cross-cut the alteration front of magnetite- and sulfide-enriched dolomite marble towards calcite marble at a 90° angle (Fig. 2).

The feldspar ± quartz-porphyritic intrusions are texturally and compositionally similar to subvolcanic intrusions mapped near other marble- and skarn-hosted base metal sulfide deposits in Bergslagen, such as Garpenberg (Jansson and Allen 2011) and Falun (Kampmann et al. 2015) (Fig. 1). Similar to the situation in the Sala area, feldspar ± quartz-porphyritic intrusions at these deposits cross-cut hydrothermally altered rocks, and have similarly yielded radiometric ages at around 1.89 Ga that overlap within error both with the intruded metavolcanic rocks, and the earliest GDG granitoids. At Sala, this relationship is illustrated by the c. 1894 ± 2 Ma age of a volcaniclastic interbed in the Sala limestone (Fig. ESM1) reported by Stephens et al. (2009), which overlap within error with the age of the Stråbruken porphyry. Hence, these relationships are consistent with alteration and mineralization already at the synvolcanic stage at c. 1.89 Ga, after build up of the stratigraphy, but prior to the emplacement of the intrusions. The absence of porphyritic intrusions within the GDG rocks east of Sala (Ripa et al. 2002) suggests that the porphyritic rocks predate the Sala granite.

Based on detailed facies analysis of the Sala limestone, Allen et al. (2003) concluded that the stromatolites at Sala formed in the photic zone at water depths no greater than 200 m. The several 100 m thickness of the Sala limestone was interpreted as reflecting a dynamic interplay between stromatolite growth up to wave base, and basin subsidence and generation of new accommodation space due to extension and subsidence. The scarcity of felsic interbeds

testifies to that the Sala limestone formed at a period when the basin experienced only intermittent volcanic activity. The stratigraphic results obtained in this study contrast with those of Ripa et al. (2002), who regarded the volcaniclastic rocks SW and NW of the Sala limestone as older. In contrast, we find that the UNIT1 polymict breccia and UNIT 2 feldspar + quartz-phyric pumice breccia stratigraphically overlie the limestone (Fig. 2), and indicate intensification of volcanic activity and cessation of stromatolite growth. The occurrence of normal grading in UNIT 1 and cross-stratification in UNIT3A-B (Fig. ESM6F) testify to sedimentation and reworking in a marine environment (McPhie 1993; Allen et al. 1996). Marine depositional conditions were thus maintained despite the deposition of several 100 m of pyroclastic material on top of the Sala limestone, further emphasizing the extensional regime.

The southwards convergence of the zones of magnetite- and sulfide-enriched dolomite marble suggest that the Zn-Pb-Ag deposits formed in the southern part of the area formed in response to hydrothermal solutions moving through the dolomitic marble from south to north during the main period of felsic volcanism and before regional metamorphism and deformation. However, the truncated nature of the alteration system against the Sala granite precludes tracing the hydrothermal system any further towards a potential source.

Mechanisms of ore and skarn formation

Alteration and mineralization predated D_1 deformation at c. 1.87 Ga and M_1 regional metamorphism at c. 1.86 Ga based on the observations above. A critical question is whether the currently observed skarn minerals formed already in conjunction with the mineralizing event at c. 1.89 Ga, or later when regional metamorphic processes overprinted the deposit.

Textural evidence suggests that base metal sulfide deposition superseded the formation of ferroan diopside and grossular-andradite (Fig. 5A–F, Fig. 6A–B), which are spatially restricted to the central parts of the alteration envelopes and occur as gangue to the stratabound Zn-Pb-Ag mineralization (Fig. ESM10B, D). In detail, the earliest sphalerite and galena formed after the deposition of blocky, euhedral ferroan diopside (Fig. 5A, D–E), which overgrew earlier, barren massive to bladed clinopyroxene skarns (Fig. 5B–D). This paragenetically late ferroan diopside directly borders sulfides and is the most Mn-rich variety encountered (Fig. 5A, E).

These anhydrous skarn minerals, as well as forsterite in the magnetite- and sulfide-enriched dolomite marble, are highly subordinate to hydrous minerals, such as tremolite-actinolite, phlogopite, serpentine, chlorite, and talc, that are commonly observed to overgrow and replace the anhydrous silicates (e.g. Figures 5A, F, 6B, ESM13A).

The latter minerals dominate the alteration envelope and gangue, together with calcite and ubiquitous trace to minor magnetite.

A metasomatic rather than metamorphic origin is supported by the poor fit between $\delta^{18}O_{V-SMOW}$ and $\delta^{13}C_{V-PDB}$ isotope data to batch and Rayleigh decarbonation models (Fig. 12F). The $\delta^{18}O_{V-SMOW}$ and $\delta^{13}C_{V-PDB}$ data distribution is instead easier to reconcile with infiltration of high-temperature fluids at significantly lower $\delta^{18}O_{V-SMOW}$ and $\delta^{13}C_{V-PDB}$ than the dolomite marble. This scenario would be more favorable for growth of the anhydrous minerals, owing to external infiltration of water (open system conditions). Infiltration metasomatism may have been facilitated by fluids flowing along the SSZ, and spreading laterally along the lithological contacts defined by felsic interbeds, forming the stratabound zones of magnetite- and sulfide-enriched dolomite.

A metasomatic mode of skarn is also consistent with textural features in the anhydrous skarn minerals, such as the oscillatory and complex growth zoning in garnet and clinopyroxene (Figs. 5A, C, 6B, C, E). This suggests a dynamic fluid infiltration history involving fluid pulses of frequently varying composition and dissolution-reprecipitation, which is a typical feature of metasomatic skarn systems (e.g. Jamtveit et al. 1993; Meinert et al. 2005). The relationships in Fig. 5A–E are consistent with a somewhat irregular trend of generally increasing hedenbergite and johannsenite components with time during formation of clinopyroxene skarns.

Whereas textural evidence suggests an intimate association between formation of hydrous magnesium silicates and base metal sulfides in the Zn-Pb-Ag deposits, similar hydrous silicates occur regionally in dolomite marble in the Sala area, complicating detailed interpretation. However, the presented mineral chemical data provides tools that aid in distinguishing ore-related hydrous silicates, e.g. the elevated contents of Fe, Mn, and locally F and Ba. The serpentine-, talc-, tremolite-, and chlorite-rich hydrous associations accompanying the ores can be interpreted to indicate a decrease in temperature and XCO_2 in relation to the formation temperature of diopside and forsterite (cf. Harris and Einaudi 1982). The observed association of tremolite, phlogopite, talc, and serpentine to base metal sulfides (e.g. Figures 5F, 9A–D, ESM13A-C) indicates that this drop coincided temporally and spatially with infiltration of a metalliferous fluid, and involved CaO-depletion (Fig. ESM13B-C). Phlogopite may have formed around the same time as tremolite based on textural relationships (intergrowths) and a similar enrichment in Ba and F (ESM4). It is inferred that the CaO-depleted serpentine-, talc-, and chlorite-rich rocks of the SSZ in the center of the Sala deposit reflect the final stages of this alteration sequence. This zonation is in agreement with the results of fluid-rock interaction modelling by Reed

(1997), involving a weakly acidic, Zn + Pb-bearing, high temperature (300 °C) mineralizing fluid interacting with dolomitic marble.

The subordinate volume of anhydrous skarns and the widespread hydrolytic alteration and hydration are characteristic features of shallow metasomatic skarn deposits (Meinert et al. 2005). This fits well with the inferred early timing of mineralization, prior to emplacement of porphyritic intrusions. Owing to the strong dependence of low pH for solubility of Zn and Pb in H_2S-bearing hydrothermal fluids (Cooke et al. 2000), hydrolytic alteration can explain the association of sphalerite and galena with amphiboles replacing clinopyroxene. However, textural evidence for earlier clinopyroxene and olivine is only present in some of the tremolite-rich skarns, possibly due to the process having gone to completion in most places. In line with modelling by Reed (1997), tremolite, talc, and serpentine can also have formed by direction replacement of dolomite by a SiO_2-bearing hydrothermal fluid.

The $\delta^{34}S_{V-CDT}$ value close to 0‰ is consistent with a primordial volcanic or magmatic-hydrothermal sulfur source (Ohmoto and Goldhaber 1997). The range in $\delta^{34}S$ in Sala sulfides falls within -5 to $+5$, which is typical of Zn skarn deposits (Bowman 1998; Ault 2004). Nevertheless, spatial variations within and between deposits indicate isotopic fractionation (Fig. ESM14). Sulfur isotopic fractionation temperatures of 378–581° were determined for sphalerite-galena pairs in ESM5 by using the equilibrium isotopic fractionation factors in Ohmoto and Rye (1979), but are anomalously high in relation to both the local metamorphic grade and typical temperatures involved in the formation of Zn deposits, including Zn skarn deposits (Zhao et al. 2003; Meinert et al. 2005). Hence, equilibrium S isotope fractionation is unlikely. The $\delta^{34}S_{V-CDT}$ zonation at the Sala deposit (Fig. ESM14) may reflect a role of mass-dependent, kinetic isotope fractionation, assuming mineralization occurred from south to north, depositing sulfides with progressively higher $\delta^{34}S_{V-CDT}$.

Sulfate-sulfide equilibria are more informative for constraining temperatures (Rye 2005), yet no evidence for sulfate-sulfide pairs in textural equilibria was found at Sala. Barite form inclusions in garnet predating sphalerite and galena, and the latter minerals area observed to vein and replace barite (Figs. ESM10 and ESM13). Hence, barite must have formed early in the alteration system, prior to the anhydrous skarns, but the origin of the barite sulfur is unclear. The low $\delta^{34}S$ values are inconsistent with SO_4^{2-} derivation from c. 1.9 Ga seawater, using the 17‰ value of Claypool et al. (1980). The 6.00–7.17‰ range in $\delta^{34}S_{V-CDT}$ is easier to explain if the barite contain a significant component of hydrothermal sulfur which was oxidized in the peripheral part of the hydrothermal system (Rye 2005), e.g. during mixing with oxygenated seawater. Barite

may either have formed during an earlier hydrothermal event, or earlier during build up of the hydrothermal system.

Kieft et al. (1987) noted lamellar intergrowths between allargentum and antimonial silver or amalgam that formed from unknown precursors of inferred higher temperature stability and concluded that there had been widespread re-equilibration of the Ag-bearing minerals at temperatures well below 280 °C. Consideration of the local and regional tectonic evolution places these processes well after the mineralizing event at c. 1.89 Ga, since the assemblages studied by Kieft et al. (1987) would not have survived regional metamorphism. Instead, the local occurrence of Ag, Sb, and Hg minerals in veinlets and fractures is consistent with local remobilization in conjunction with retrograde regional metamorphism later during the Svecokarelian orogeny, as has been inferred elsewhere in Bergslagen (Wagner et al. 2005; Andersson et al. 2016; Tiu et al. 2021). As shown by Wagner et al. (2005) and Tiu et al. (2021), sulphosalts including freibergite and boulangerite are commonly remobilized during metamorphism. Such a secondary origin may explain why the $\delta^{34}S_{V-CDT}$ values of the sulphosalts at Sala mine differ from directly adjacent sulfides (Fig. ESM14).

Comparison with Zn skarn deposits

The results of this study suggest that the Zn-Pb-Ag deposits in the Sala area can be classified as Zn skarn deposits, but also highlight a number of unusual features. These include (1) formation of the deposits in a sub-seafloor setting in an actively subsiding marine basin with intense calc-alkaline felsic magmatism (Allen et al. 1996; Stephens et al. 2009), (2) lack of minerals containing essential manganese in the skarns, and (3) abundance of magnesian silicates.

These points are inter-related in the sense that dolomitization likely reflects a shallow marine setting, in which seawater may have been important in driving sub-seafloor dolomitization of stromatolitic limestone (Jansson et al. 2017). Dolomitization prior to the skarn-forming event is likely the main reason for the more magnesian skarns at Sala in comparison with Zn skarn deposits worldwide, in which Fe + Mn-silicates predominate (Meinert et al. 2005). Nevertheless, an increase in the Fe + Mn component in silicates is observed with increasing degree of skarn alteration at Sala: the grossular-andradite- and ferroan diopside-rich skarns have a higher Fe + Mn component than the forsterite-bearing rocks in the magnetite- and sulfide-enriched dolomite marble. This zonation is opposite to that in many skarn deposits, where magnesian silicates are characteristic of a proximal setting in relation to specific causative intrusions (Harris and Einaudi 1982; Newberry et al. 1991; Einaudi et al. 2000; Meinert et al. 2005). The zonation from ore to magnetite- and sulfide-enriched dolomite marble can be attributed to the shift from a fluid-buffered to a dolomite-buffered

environment with increasing distance from fluid conduits, rather than with distance from specific intrusions.

Cross-cutting relationships indicate that the mapped intrusions post-date the main stages of alteration and mineralization, and no specific causative intrusive body can be defined in the Sala area. This feature is characteristics of Zn skarn deposits, which commonly formed distal to causative intrusions (Meinert et al. 2005). It is emphasized that the stratigraphic footwall of the Sala limestone was removed during the emplacement of the Sala granite. At least at the current level of exposure, this precludes tracing the hydrothermal system any further towards a potential source.

Conclusions

This study supports earlier conclusions by Jansson and Allen (2013, 2015) that contact metasomatic processes were involved in the formation of stratabound Zn-Pb-Ag deposits in Bergslagen at c. 1.89 Ga. The stratabound Zn-Pb-Ag deposits in the Sala area formed at c. 1.89 Ga in a sub-seafloor setting in an actively subsiding marine basin on extended continental crust. Extension led to subsidence and burial, but also emplacement of granitic melts to shallow crustal levels. The early stage of this burial and intrusive history involved seawater- or brine-driven alteration, including dolomitization of stromatolitic limestone. Subsequent alteration involved higher temperature hydrothermal fluids enriched in base metals, iron, manganese, and sulfur, which were focused along lithological contacts and faults. Textural evidence suggests that the skarn-forming mineralizing system evolved from formation of complexly zoned, granoblastic, or bladed clinopyroxene, to formation of coarser-grained ferroan diopside and andradite-grossular garnet before sulfide mineralization. Sphalerite-galena-rich sulfide mineralization was temporally coincident with later, more hydrous associations of phlogopite, tremolite-actinolite, chlorite, serpentine, magnetite, and calcite. Mineralization is interpreted to have formed during a transition from high-T metasomatism to hydrolytic alteration.

The driving agents of the alteration and mineralization were most likely heat derived from a more deeply seated calc-alkaline granitic magmatic system, members of which intruded the alteration system with time. An average $\delta^{34}S_{V\text{-}CDT}$ of $+1.6 \pm 1.9‰$ in sulfides and observed negative shifts in $\delta^{18}O_{V\text{-}SMOW}$ and $\delta^{13}C_{V\text{-}PDB}$ in dolomite marble are consistent with a direct magmatic-hydrothermal input of fluids and sulfur, albeit not diagnostic. Alternative interpretations include (1) derivation of sulfur from leached volcanic rocks and (2) negative shifts in $\delta^{18}O_{V\text{-}SMOW}$ due to interaction with heated seawater. Both options are feasible in light of the geological setting of Bergslagen at 1.89 Ga.

The unusually Mg-rich mineralogy in relation to Zn skarns worldwide is interpreted to reflect the dolomitic precursor. The synvolcanic timing and marine back-arc setting with intense volcanism is somewhat unusual in relation to typical Zn skarn deposits worldwide as summarized by Meinert et al. (2005). Besides presenting stronger evidence for the presence of pre-metatmorphic, c. 1.89 Ga skarn deposits in Bergslagen, the results of this study extend the search space of Zn skarn deposits to similar successions and tectonic settings in other parts of the world.

References

Allen R, Bull S, Ripa M, Jonsson R (2003) Regional stratigraphy, basin evolution, and the setting of stratabound Zn–Pb–Cu–Ag–Au deposits in Bergslagen, Sweden. Final report for SGU-FoU project:03–1203.

Allen RL, Lundström I, Ripa M, Christofferson H (1996) Facies analysis of a 1.9 Ga, continental margin, back-arc, felsic caldera

province with diverse Zn-Pb-Ag-(Cu-Au) sulfide and Fe oxide deposits, Bergslagen region. Sweden Economic Geology 91:979–1008

Andersson SS, Jonsson E, Hogdahl K (2016) Metamorphism and deformation of a Palaeoproterozoic polymetallic sulphide-oxide mineralisation: Hornkullen, Bergslagen, Sweden. GFF 138:410–423

Ault K (2004) Sulfur and lead isotope study of the El Mochito Zn-Pb-Ag deposit. Econ Geol 99:1223–1231

Barton MD, Young S (2002) Non-pegmatitic deposits of beryllium: mineralogy, geology, phase equilibria and origin. Rev Mineral Geochem 50:591–691

Bowman J (1998) Stable isotope systematics of skarns: Mineralogical Association of Canada Short Course Series, v. 26.

Burisch M, Gerdes A, Meinert LD, Albert R, Seifert T, Gutzmer J (2019) The essence of time–fertile skarn formation in the Variscan Orogenic Belt. Earth Planet Sci Lett 519:165–170

Claypool GE, Holser WT, Kaplan IR, Sakai H, Zak I (1980) The age curves of sulfur and oxygen isotopes in marine sulfate and their mutual interpretation. Chem Geol 28:199–260

Collini B (1965) En stromatolitförekomst i Mellansveriges urberg. Geologi 17:9-10

Cooke DR, Bull SW, Large RR, McGoldrick PJ (2000) The importance of oxidized brines for the formation of Australian Proterozoic stratiform sediment-hosted Pb-Zn (Sedex) deposits. Econ Geol 95:1–18

Doyle MG, Allen RL (2003) Subsea-floor replacement in volcanic-hosted massive sulfide deposits. Ore Geol Rev 23:183–222

Einaudi M, Dilles H, Barton M, Johnson D, Proffett J (2000) Skarns of the Yerington district, Nevada: a triplog and commentary. Contrast Styles of Intrusion-Associate Hydrotherm Syst: Soc Econ Geol Guidebook Series 32:101–125

Franklin J, Gibson H, Jonasson I, Galley A (2005) Volcanogenic massive sulfide deposits. Economic Geology 100th anniversary volume 98:523–560.

Gnos E, Armbruster T (2000) Kinoshitalite, Ba (Mg) 3 (Al2Si2) O10 (OH, F) 2, a brittle mica from a manganese deposit in Oman: paragenesis and crystal chemistry. Am Mineral 85:242–250

Grip E (1983) Malmstyrande strukturer i Bergslagen. Del 2, Detaljrapport med kartor. Svenska Gruvföreningen.

Harris NB, Einaudi MT (1982) Skarn deposits in the Yerington District, Nevada; metasomatic skarn evolution near Ludwig. Econ Geol 77:877–898

Hermansson T, Stephens MB, Corfu F, Page LM, Andersson J (2008) Migratory tectonic switching, western Svecofennian orogen, central Sweden: constraints from U/Pb zircon and titanite geochronology. Precambrian Res 161:250–278. https://doi.org/10.1016/j.precanires.2007.08.008

Hey MH (1954) A new review of the chlorites. Mineral Mag J Mineral Soc 30:277–292

Irvine T, Baragar W (1971) A guide to the chemical classification of the common volcanic rocks. Can J Earth Sci 8:523–548

Jamtveit B, Wogelius RA, Fraser DG (1993) Zonation patterns of skarn garnets: records of hydrothermal system evolution. Geology 21:113–116

Jansson N (2007) A structural and ore geological study of the Palaeoproterozoic Stratabound Sala Zn-Pb-Ag deposit, Bergslagen. Examensarbete vid institutionen för geovetenskaper, Uppsala, Sweden

Jansson N, Zetterqvist A, Allen R, Billström K, Malmström L (2017) Genesis of the Zinkgruvan stratiform Zn-Pb-Ag deposit and associated dolomite-hosted Cu ore, Bergslagen, Sweden. Ore Geol Rev 82:285–308

Jansson NF, Allen RL (2011) Timing of volcanism, hydrothermal alteration and ore formation at Garpenberg, Bergslagen, Sweden. GFF 133:3–18. https://doi.org/10.1080/11035897.2010.547597

Jansson NF, Allen RL (2013) Timing and setting of skarn and iron oxide formation at the Smaltarmossen calcic iron skarn deposit, Bergslagen, Sweden. Miner Deposita 48:313–339

Jansson NF, Erismann F, Lundstam E, Allen RL (2013) Evolution of the Paleoproterozoic volcanic-limestone-hydrothermal sediment succession and Zn-Pb-Ag and iron oxide deposits at Stollberg, Bergslagen region, Sweden. Econ Geol 108:309–335. https://doi.org/10.2113/econgeo.108.2.309

Jansson NF, Allen RL (2015) Multistage ore formation at the Ryllshyttan marble and skarn-hosted Zn-Pb-Ag–(Cu) plus magnetite deposit, Bergslagen, Sweden. Ore Geol Rev 69:217–242. https://doi.org/10.1016/j.oregeorev.2015.02.018

Jansson NF (2017) Structural evolution of the Palaeoproterozoic Sala stratabound Zn-Pb-Ag carbonate-replacement deposit, Bergslagen, Sweden. GFF 139:21–35

Kampmann TC, Stephens MB, Ripa M, Hellstrom FA (2015) Timing of magmatism and mineralisation at Falun, a major base metal sulphide deposit in the Fennoscandian Shield, Sweden. Mineral Res Sustain World 1–5:591–594

Kampmann TC, Jansson NF, Stephens MB, Majka J, Lasskogen J (2017) Systematics of hydrothermal alteration at the Falun base metal sulfide deposit and implications for ore genesis and exploration, Bergslagen ore district, Fennoscandian Shield, Sweden. Econ Geol 112:1111–1152

Kieft C, Holmgren J, Eriksson G (1987) The silver-mercury-antimony minerals of Sala, Sweden. Can Mineral 25:647–658

Klein C (1973) Changes in mineral assemblages with metamorphism of some banded Precambrian iron-formations. Econ Geol 68:1075–1088

McPhie J (1993) Volcanic textures: a guide to the interpretation of textures in volcanic rocks.

Meinert L, Dipple G, Nicolescu S (2005) World skarn deposits. Economic Geology 100th Anniversary Volume.

Meinert LD (1987) Skarn zonation and fluid evolution in the Groundhog mine, Central mining district, New Mexico. Econ Geol 82:523–545

Middlemost EA (1994) Naming materials in the magma/igneous rock system. Earth Sci Rev 37:215–224

Newberry RJ, Einaudi MT, Eastman HS (1991) Zoning and genesis of the Darwin Pb-Zn-Ag skarn deposit, California; a reinterpretation based on new data. Econ Geol 86:960–982

Ohmoto H, Rye R (1979) Isotopes of sulfur and carbon. in ''Geochemistry of hydrothermal ore deposits'', HL Barnes ed. Wiley.

Ohmoto H, Goldhaber M (1997) Sulfur and carbon isotopes. Pp. 517À612 in: Geochemistry of hydrothermal ore deposits 3rd edition (HL Barnes, editor). Wiley, New York.

Reed MH (1997) Hydrothermal alteration and its relationship to ore fluid composition. Geochem Hydrotherm Ore Deposits 1:303–365

Ripa M, Kübler L, Persson L, Göransson M (2002) Beskrivning till berggrundskartan 11G Västerås NO. Geological Survey of Sweden Af:70.

Rye RO (2005) A review of the stable-isotope geochemistry of sulfate minerals in selected igneous environments and related hydrothermal systems. Chem Geol 215:5–36

Sangster DF (2020) Evidence that Broken Hill-type Pb-Zn deposits are metamorphosed SEDEX deposits. Miner Deposita 55:1263–1270

Shields G, Veizer J (2002) Precambrian marine carbonate isotope database: Version 1.1. Geochemistry, Geophysics, Geosystems 3:1 of 12–12 of 12.

Sjögren H (1910) The Sala mine. Geologiska Föreningen i Stockholm Förhandlingar 32:1363–1396

Söderlund U, Isachsen CE, Bylund G, Heaman LM, Patchett PJ, Vervoort JD, Andersson UB (2005) U–Pb baddeleyite ages and Hf, Nd isotope chemistry constraining repeated mafic magmatism in the Fennoscandian Shield from 1.6 to 0.9 Ga. Contributions to Mineralogy and Petrology 150:174.

Spry PG, Teale GS (2021) A classification of Broken Hill-type deposits: a critical review. Ore Geology Reviews:103935.

Stephens MB, Ripa M, Lundström I, Persson L, Bergman T, Ahl M, Wahlgren CH, Persson PH, Wickström L (2009) Synthesis of the bedrock geology in the Bergslagen region, Fennoscandian Shield, south-central Sweden. Geological Survey of Sweden, Uppsala, pp 259.

Stephens MB, Bergman S (2020) Regional context and lithotectonic framework of the 2.0–1.8 Ga Svecokarelian orogen, eastern Sweden. Geol Soc, London, Memoirs 50:19–26

Stephens MB, Jansson NF (2020) Paleoproterozoic (1.9–1.8 Ga) syn-orogenic magmatism, sedimentation and mineralization in the Bergslagen lithotectonic unit, Svecokarelian orogen. Geol Soc, London, Memoirs 50:155–206

Taylor Jr H (1986) Igneous rocks: I. Process of isotopic fractionation and isotope systematics. Stable isotopes in high temperature geological processes.

Tegengren F (1924) Sveriges ädlare malmer och bergverk. Sveriges Geologiska Undersökning, Series Ca No. 17.

Tiu G, Jansson N, Wanhainen C, Ghorbani Y, Lilja L (2021) Ore mineralogy and trace element (re) distribution at the metamorphosed Lappberget Zn-Pb-Ag-(Cu-Au) deposit, Garpenberg, Sweden. Ore Geology Reviews:104223.

Tornos F, Peter JM, Allen R, Conde C (2015) Controls on the siting and style of volcanogenic massive sulphide deposits. Ore Geol Rev 68:142–163

Turner T (2020) Petrography, alteration and structure of the Bronäs Zn-Pb-Ag deposits. Bergslagen, Sweden

Valley J (1986) Stable isotope geochemistry of metamorphic rocks. Rev Mineral 16:445–489

Wagner T, Jonsson E, Boyce AJ (2005) Metamorphic ore remobilization in the Hallefors district, Bergslagen, Sweden: constraints from mineralogical and small-scale sulphur isotope studies. Miner Deposita 40:100–114

Zhao Y, Dong Y, Li D, Bi C (2003) Geology, mineralogy, geochemistry, and zonation of the Bajiazi dolostone-hosted Zn–Pb–Ag skarn deposit, Liaoning Province, China. Ore Geol Rev 23:153–182

Publisher's note Springer Nature remains neutral with regard to jurisdictional claims in published maps and institutional affiliations.